

Expanding the Sample: The Relationship Between the Black Hole Mass of BCGs and the Total Mass of Galaxy Clusters

FREDERIKA PHIPPS,^{1,2} ÁKOS BOGDÁN,² LORENZO LOVISARI,² ORSOLYA E. KOVÁCS,^{2,3,4} MARTA VOLONTERI,⁵ AND YOHAN DUBOIS⁵

¹*School of Physics and Astronomy, University of Southampton, Southampton, SO17 1BJ, United Kingdom*

²*Harvard-Smithsonian Center for Astrophysics, 60 Garden Street, Cambridge, MA 02138, USA*

³*Konkoly Observatory, MTA CSFK, H-1121 Budapest, Konkoly Thege M. út 15-17, Hungary*

⁴*Eötvös University, Department of Astronomy, Pf. 32, 1518, Budapest, Hungary*

⁵*Institut d'Astrophysique de Paris, Sorbonne Universités, UPMC Univ Paris 6 et CNRS, UMR 7095, 98 bis bd Arago, F-75014 Paris, France*

ABSTRACT

Supermassive Black Holes (BHs) residing in brightest cluster galaxies (BCGs) are overly massive when considering the local relationships between the BH mass and stellar bulge mass or velocity dispersion. Due to the location of these BHs within the cluster, large-scale cluster processes may aid the growth of BHs in BCGs. In this work, we study a sample of 71 galaxy clusters to explore the relationship between the BH mass, stellar bulge mass of the BCG, and the total gravitating mass of the host clusters. Due to difficulties in obtaining dynamically measured BH masses in distant galaxies, we use the Fundamental Plane relationship of BHs to infer their masses. We utilize X-ray observations taken by *Chandra* to measure the temperature of the intra-cluster medium (ICM), which is a proxy for the total mass of the cluster. We analyze the $M_{\text{BH}} - kT$ and $M_{\text{BH}} - M_{\text{bulge}}$ relationships and establish the best-fitting power laws: $\log_{10}(M_{\text{BH}}/10^9 M_{\odot}) = -0.35 + 2.08 \log_{10}(kT/1\text{keV})$ and $\log_{10}(M_{\text{BH}}/10^9 M_{\odot}) = -1.09 + 1.92 \log_{10}(M_{\text{bulge}}/10^{11} M_{\odot})$. Both relations are comparable with that established earlier for a sample of brightest group/cluster galaxies with dynamically measured BH masses. Although both the $M_{\text{BH}} - kT$ and the $M_{\text{BH}} - M_{\text{bulge}}$ relationships exhibit large intrinsic scatter, based on Monte Carlo simulations we conclude that dominant fraction of the scatter originates from the Fundamental Plane relationship. We split the sample into cool core and non-cool core resembling clusters, but do not find statistically significant differences in the $M_{\text{BH}} - kT$ relation. We speculate that the overly massive BHs in BCGs may be due to frequent mergers and cool gas inflows onto the cluster center.

Keywords: clusters: general — clusters: intracluster medium — galaxies: elliptical and lenticular, cD — galaxies: evolution — X-rays: clusters

1. INTRODUCTION

Throughout the evolution of galaxies, they undergo diverse physical processes, which produce the observed galaxy populations and result in various relations between different galaxy properties (Croton et al. 2006; Faber et al. 2007). BHs are believed to have a profound effect on the evolution of their host galaxy due to their energetic feedback (Richstone et al. 1998; Cattaneo et al. 2009; Cheung et al. 2016). By precisely measuring the mass of BHs, relationships between the BH mass and the properties of the host galaxies have been established, the most well-known being the corre-

lation between central stellar velocity dispersion (σ) and BH mass (e.g. Ferrarese & Merritt 2000; Gebhardt et al. 2000; McConnell & Ma 2013; DeGraf et al. 2015), as well as the relationship between stellar bulge mass and BH mass (e.g. Magorrian et al. 1998; Häring & Rix 2004). These results have contributed to the development of the current theoretical paradigm, in which the BH and the host galaxies co-evolve and regulate each others growth (Fabian 1999; King 2003; DiMatteo et al. 2005; Hopkins et al. 2006; Shankar et al. 2006; Somerville et al. 2008).

The study of BHs and their host galaxies has been extensive, despite the difficulties in measuring the BH

masses accurately. However, large-scale structures, in which most galaxies are embedded (Sepp & Gramann. 2013), could influence the evolution of BHs. Most galaxy groups/clusters contain a unique type of elliptical galaxy, known as the Brightest Group/Cluster Galaxies (BGGs/BCGs) at their center (Crawford et al. 1999; Bernardi et al. 2007). Typically, BGGs/BCGs are both the most massive and luminous galaxies in the group/cluster. As these galaxies are located at the bottom of the potential well for these large-scale structures, it is feasible that the BHs of BCGs undergo a different evolution than BHs residing in field or satellite galaxies. Studies of BHs in BCGs pointed out that many of these BHs are over-massive in comparison to the stellar bulge mass or velocity dispersion of the BCG (McConnell et al. 2011, 2012; Mezcua et al. 2018). This hints that the large-scale potential of clusters may aid the growth of these BHs.

There is a vast difference between the scales of BHs and galaxy groups/clusters. While the sphere of influence of BHs is ~ 100 pc for BHs with masses $\sim 10^9 M_\odot$, galaxy groups/clusters extend to Mpc scales. Therefore, it is appealing to probe if the growth of BHs in BCGs may be influenced by the large-scale structures. From theoretical considerations, a correlation between BH mass and cluster halo temperature is expected (Gaspari & Sadowski 2017). This relation had been previously quantified by Mittal et al. (2009), who used the luminosity of the BCG as a proxy for the BH mass. More recently, Bogdán et al. (2018) investigated using a sample of 17 galaxy groups/clusters, which had dynamically measured BHs in their BGGs/BCGs. By analyzing *XMM-Newton* X-ray observations, they found a tight correlation between the BH and total mass of the group/cluster, which was traced via the gas temperature of the ICM. This relation had an intrinsic scatter in the x and y-axes of 0.22 and 0.38. They concluded that the $M_{\text{BH}} - kT$ relation is tighter and has less scatter than the $M_{\text{BH}} - M_{\text{bulge}}$ relation (which had scatter of 0.35 and 0.68 in each axes), hinting that the BH mass of BGGs/BCGs may be determined by physical processes that are governed by the properties of the large-scale potential. The results of Bogdán et al. (2018) have been successfully reproduced in simulations (Bassini et al. 2019). However, the sample of Bogdán et al. (2018) was relatively small, as it was limited

by the available dynamical BH mass measurements in BGGs/BCGs. Whilst this means their masses are more accurate, this also meant that they were unable to investigate these relationships for a notable sample of massive clusters. To further probe the findings of Bogdán et al. (2018), it is necessary to extend the sample of galaxy groups and clusters, especially including massive systems.

As measuring the mass of BHs using dynamical methods is challenging for less massive and/or distant BHs, we must rely on tracers. In this work, we utilize the Fundamental Plane relationship, which defines a plane between BH mass and its luminosity in the X-ray and radio (Merloni et al. 2003; Falcke et al. 2004; Körding et al. 2006; Gültekin et al. 2009). The Fundamental Plane relationship for BCGs was investigated by Hlavacek-Larrondo et al. (2012) for a sample of 18 BCGs. This work was extended by Mezcua et al. (2018), who measured the X-ray and radio properties for a large sample of BHs in BCGs using *Chandra* and *VLBI* data. Here, we use their results to infer both BH masses and bulge masses of the BCGs. While they investigated the Fundamental Plane relationship of both Merloni et al. (2003) and Plotkin et al. (2012), in this work we opt to use the “standard” relation of Merloni et al. (2003) as this relation covers the largest range of radio luminosities and BH masses.

To derive the total mass of the galaxy clusters, we utilize *Chandra* X-ray observations. Specifically, the temperature of the ICM is a good proxy for the cluster’s total mass (Horner et al. 1999; Ettori et al. 2013). Not only is it a good proxy, but through using this method we maintain a straight forward comparison with the work of Bogdán et al. (2018). We then use the temperature measured from these X-ray observations to study the BH mass – cluster temperature relationship.

The structure of the paper is as follows: in Section 2 we discuss the sample selection process and the observations used to obtain them. Section 3 describes the analysis of the *Chandra* data. Results are presented in Section 4 and in Section 5 we discuss the implications of these results. We summarize our results in Section 6. In this paper, we take the Hubble constant, H_0 , to be $70 \text{ km s}^{-1} \text{ Mpc}^{-1}$ and $\Omega_M = 0.3$ and $\Omega_\Lambda = 0.7$. All error bars represent 1σ uncertainties, unless otherwise mentioned.

Table 1. Analyzed *Chandra* observations in this work.

Name	Obsid	Instrument	redshift	t_{total} (ks)	t_{clean} (ks)	Date
A1204	2205	ACIS-I	0.171	23.6	20.3	2001 Jun 01
A1367	514	ACIS-S	0.022	40.5	31.1	2000 Feb 26
	17201	ACIS-I	0.022	61.3	48.5	2016 Jan 31
A1446	4975	ACIS-S	0.103	58.4	49.3	2004 Sep 29
A1644	7922	ACIS-I	0.048	51.5	40.1	2007 May 24
A1664	7901	ACIS-S	0.128	36.6	30.0	2006 Dec 04
A168	3203	ACIS-I	0.044	40.6	31.3	2002 Feb 05
A1763	3591	ACIS-I	0.228	19.6	17.0	2003 Oct 28
A1795	493	ACIS-S	0.063	19.6	14.4	2000 Mar 21
A1930	11733	ACIS-S	0.132	34.5	25.9	2010 Sep 09
A2009	10438	ACIS-I	0.153	19.9	8.88	2008 Dec 04
A2029	4977	ACIS-S	0.078	77.9	57.0	2004 Jan 08
A2033	15167	ACIS-I	0.078	8.97	8.59	2013 May 22
A2052	5807	ACIS-S	0.036	127.0	101.0	2006 Mar 24
	10478	ACIS-S	0.036	119.1	101.5	2009 May 25
A2063	4187	ACIS-I	0.034	8.8	1.4	2003 Apr 20
A2110	15160	ACIS-I	0.098	7.98	7.00	2013 Aug 29
A2199	10748	ACIS-I	0.031	40.6	36.2	2009 Nov 19
A2204	7940	ACIS-I	0.151	77.1	63.7	2007 Jun 06
A2355	15097	ACIS-I	0.231	19.8	14.7	2013 Nov 05
A2390	4193	ACIS-S	0.233	95.1	69.0	2003 Sep 11
A2415	12272	ACIS-I	0.057	9.92	7.90	2010 Sep 24
A2597	7329	ACIS-S	0.083	60.1	43.6	2006 May 04
A262	7921	ACIS-S	0.017	111.0	92.1	2006 Nov 20
	2215	ACIS-S	0.017	28.7	24.4	2001 Aug 03
A2626	16136	ACIS-S	0.055	111.0	86.3	2013 Oct 20
A2634	4816	ACIS-S	0.030	49.5	39.7	2004 Aug 31
A2665	12280	ACIS-I	0.057	9.92	5.92	2011 Jan 17
A2667	2214	ACIS-S	0.235	9.65	9.05	2001 Jun 19
A3017	15110	ACIS-I	0.220	14.9	12.0	2013 May 01
A3526	16223	ACIS-S	0.010	179.0	145.0	2014 May 26
A3528S	8268	ACIS-I	0.057	8.08	8.07	2007 Mar 20
A3581	12884	ACIS-S	0.022	84.5	68.7	2011 Jan 03
	1650	ACIS-S	0.022	7.2	7.0	2001 Jun 07
A3695	12274	ACIS-I	0.089	9.87	9.37	2010 Aug 17
A4059	5785	ACIS-S	0.049	92.1	83.3	2005 Jan 26
	897	ACIS-S	0.049	40.7	6.5	2000 Sep 24
A478	1669	ACIS-S	0.086	42.4	31.2	2001 Jan 27
A496	4976	ACIS-S	0.033	75.1	36.5	2004 Jul 22
AS1101	11758	ACIS-I	0.056	97.7	79.6	2009 Aug 24

Table 1 continued

Table 1 (*continued*)

AS780	9428	ACIS-S	0.234	39.6	34.6	2008 Jun 16
AS851	11753	ACIS-I	0.010	72.6	64.7	2009 Aug 19
Hercules	5796	ACIS-S	0.155	47.5	43.2	2005 May 09
Hydra	4970	ACIS-S	0.055	98.8	86.7	2004 Oct 22
RXJ0058.9+2657	6830	ACIS-I	0.048	94.4	78.2	2006 Sep 02
RXJ0107.4+3227	2147	ACIS-S	0.018	44.4	33.2	2000 Nov 06
RXJ0123.6+3315	2882	ACIS-I	0.017	43.6	33.9	2002 Jan 08
RXJ0341.3+1524	4182	ACIS-I	0.029	23.5	22.9	2003 Mar 11
RXJ0352.9+1941	10466	ACIS-S	0.109	27.2	24.3	2008 Dec 18
RXJ0439.0+0520	9369	ACIS-I	0.245	19.9	18.7	2007 Nov 12
RXJ0751.3+5012	15170	ACIS-I	0.024	97.7	74.7	2013 May 14
RXJ0819.6+6336	2199	ACIS-S	0.119	14.9	11.3	2000 Oct 19
RXJ1050.4-1250	3243	ACIS-S	0.015	29.5	22.6	2002 Nov 05
RXJ1304.3-3031	4998	ACIS-I	0.010	15.0	13.6	2004 Feb 15
RXJ1315.4-1623	9399	ACIS-S	0.009	82.7	66.9	2008 Mar 07
	17196	ACIS-S	0.009	88.9	80.9	2015 May 11
RXJ1320.1+3308	6941	ACIS-S	0.038	38.6	31.2	2005 Nov 01
RXJ1501.1+0141	12952	ACIS-S	0.007	143.0	126.0	2011 Apr 05
	9517	ACIS-S	0.007	98.8	82.0	2008 Jun 05
RXJ1504.1-0248	5793	ACIS-I	0.217	39.2	30.7	2005 Mar 20
RXJ1506.4+0136	7923	ACIS-I	0.006	90.0	76.4	2007 Jun 12
RXJ1522.0+0741	900	ACIS-I	0.045	57.3	53.2	2000 Apr 03
RXJ1524.2-3154	9401	ACIS-S	0.102	40.9	29.4	2008 Jan 07
RXJ1539.5-8335	8266	ACIS-I	0.076	7.99	7.64	2007 Jun 24
RXJ1558.4-1410	9402	ACIS-S	0.097	40.1	31.4	2008 Apr 09
RXJ1604.9+2356	9423	ACIS-S	0.032	74.5	56.9	2008 May 18
RXJ1715.3+5725	4194	ACIS-I	0.028	47.3	25.9	2003 Sep 17
RXJ1720.1+2638	4361	ACIS-I	0.161	25.7	15.6	2002 Aug 19
RXJ1750.2+3504	12252	ACIS-I	0.171	19.8	16.8	2010 Oct 15
RXJ1844.1+4533	5295	ACIS-I	0.092	30.7	25.1	2004 Jan 29
RXJ2129.6+0005	9370	ACIS-I	0.235	29.5	27.0	2009 Apr 03
Z1665	15161	ACIS-I	0.031	9.95	7.11	2013 Feb 27
Z235	11735	ACIS-S	0.083	19.8	13.3	2009 Sep 06
Z3146	9371	ACIS-I	0.291	40.2	28.0	2008 Jan 18
Z7160	4192	ACIS-I	0.258	91.9	79.3	2003 Sep 05
Z808	12253	ACIS-I	0.169	18.8	14.3	2010 Oct 06
Z8193	14988	ACIS-S	0.175	18.2	11.8	2013 Oct 07
Z8276	11708	ACIS-S	0.075	45.4	38.9	2009 Nov 26

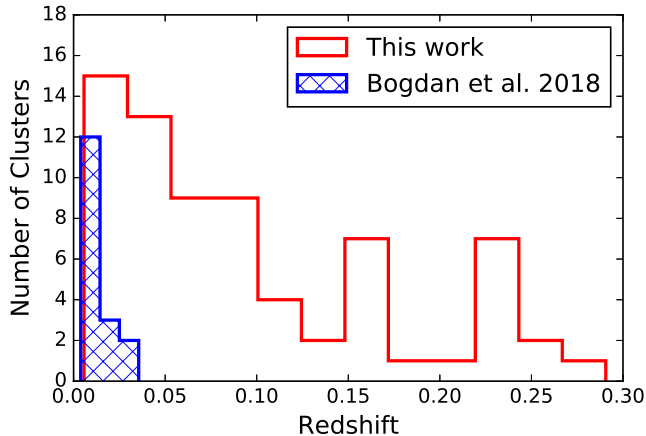


Figure 1. Redshift distribution for two cluster samples. The hatched (blue) distribution is the clusters in the sample studied by Bogdán et al. (2018). The empty (red) distribution shows the clusters studied in this work. Note that the galaxy clusters investigated in this work have significantly higher redshifts than those in Bogdán et al. (2018).

2. SAMPLE

To study a larger set of galaxy clusters with indirect BH mass measurements, we rely on Mezcua et al. (2018) who investigated the Fundamental Plane relationship for BCGs. Mezcua et al. (2018) drew their sample from Hogan et al. (2015), who examined the radio properties of X-ray selected BCGs from a parent sample of three *ROSAT* X-ray catalogs. This sample includes galaxy clusters with redshifts in the range of $0.006 < z < 0.29$. By utilizing *Chandra* X-ray and *VLBI* radio observations, Mezcua et al. (2018) probed the Fundamental Plane relationship. They inferred the BH masses of the galaxies using the K-band luminosities of the BCGs. They concluded that the BHs were overly massive compared to the galaxy's stellar mass. However, they did not expand their analysis to include the effects of the cluster. In this work, we utilize the Fundamental Plane relationship from Merloni et al. (2003), together with the X-ray and radio luminosities from Mezcua et al. (2018), in order to calculate the BH masses.

In Figure 1 we show the redshift distribution for our sample as well as that for the sample studied by Bogdán et al. (2018). Given the larger redshift range of the present sample, we can explore a larger volume, hence more massive clusters can be studied. However, while dynamically measured values for BH mass are preferable in constraining accurate relationships, they are limited to nearby and massive BHs. Therefore, without the use

of tracers we would not be able to significantly increase the sample size and explore higher redshift, and, hence more massive clusters.

3. DATA ANALYSIS

3.1. *Chandra* Data

3.1.1. Data Reduction

To study the ICM of the galaxy clusters, we utilized *Chandra* X-ray observations. All the systems have been observed with *Chandra* – as it was also used by Mezcua et al. (2018). Although *XMM-Newton* data is available for some sources in our sample, in order to avoid calibration issues (e.g. see Schellenberger et al. 2015) we opted to use only *Chandra* data. The data analysis was performed using CIAO software version 4.9 and CALDB 4.7.6 (Fruscione et al. 2006).

As the first step of the analysis, we reprocessed all *Chandra* observations using the *chandra_repro* tool. Since we aim to study the diffuse emission, we must identify and remove bright point sources. To this end, we utilized the *wavdetect* task, which correlates the data with a Mexican Hat wavelet function of different scales and generates a list of point sources. The applied scales were the square root series of two from $\sqrt{2}$ to 8.0. The point sources found by *wavdetect* were then masked from the analysis of the diffuse X-ray emission.

Once the point sources were excluded, we filtered the time periods that had high background due to flares. For each observation, we extracted light curves in the 2.3–7.3 keV energy range and binned them with a time interval of 200 s. Light curves were extracted within this energy range, as *Chandra* is most sensitive to flares in this band (Hickox & Markevitch 2006). We applied the *deflare* tool with the parameter $n\sigma = 2$. Hence, we removed all time periods that were $\geq 2\sigma$ outliers from the mean, which resulted in exposures that were typically 15–25% shorter than the original exposures (Table 1). Although we could be less conservative by applying a 3σ clipping instead, we prefer to use a 2σ clip. We use this clipping since it is more effective in excluding soft proton flares, and therefore more effective in avoiding bias in the spectral fit procedure.

To account for the sky and instrumental background components, we constructed the blank-sky background for each observation. We used the *blanksky* tool to create the background event files. While the spectrum of the background remains invariable, its normalization exhibits variations. To account for this, we used the count rates in the 10–12 keV energy range to re-scale the blank-sky background files.

Table 2. Characteristics of the analyzed galaxy clusters, their BCGs, and BHs.

Name	N_{H} (10^{20}cm^{-2})	$\log_{10}(M_{\text{BH}})$ (M_{\odot})	$\log_{10}(M_{\text{bulge}})$ (M_{\odot})	kT (keV)	M_{500} ($10^{14} M_{\odot}$)	R_{500} (Mpc)	R_{frac}
(1)	(2)	(3)	(4)	(5)	(6)	(7)	(8)
A1204	1.38	9.01 ± 0.62	11.77 ± 0.02	2.51 ± 0.31	1.67 ± 0.18	0.716 ± 0.016	1.00
A1367*	2.39	< 11.19	11.40 ± 0.01	2.40 ± 0.07	2.11 ± 0.04	0.887 ± 0.007	0.46
A1446	1.5	10 ± 0.08	11.83 ± 0.02	3.17 ± 0.25	2.49 ± 0.17	0.867 ± 0.012	0.68
A1644*	5.19	< 10.78	12.13 ± 0.04	2.90 ± 0.11	2.14 ± 0.07	0.0867 ± 0.006	0.73
A1664*	8.72	< 10.58	11.76 ± 0.02	4.54 ± 0.42	4.60 ± 0.36	1.040 ± 0.017	0.73
A168*	3.25	< 9.14	11.76 ± 0.02	1.69 ± 0.07	0.85 ± 0.03	0.640 ± 0.005	0.58
A1763	0.92	9.94 ± 0.11	12.37 ± 0.05	5.82 ± 0.66	7.04 ± 0.68	1.101 ± 0.022	1.00
A1795*	1.17	< 10.83	12.05 ± 0.03	6.07 ± 0.35	7.56 ± 0.37	1.302 ± 0.014	0.69
A1930	1.13	9.79 ± 0.16	12.25 ± 0.05	3.34 ± 0.43	2.72 ± 0.3	0.870 ± 0.020	0.89
A2009	3.27	9.74 ± 0.08	12.17 ± 0.04	3.89 ± 0.55	3.53 ± 0.43	0.931 ± 0.024	1.00
A2029*	3.15	< 9.38	11.90 ± 0.03	8.76 ± 0.05	10.1 ± 7.7	1.415 ± 0.361	0.71
A2033	2.94	9.68 ± 0.15	12.17 ± 0.04	2.12 ± 0.23	1.25 ± 0.12	0.705 ± 0.014	0.96
A2052	2.85	11.23 ± 0.12	11.93 ± 0.03	3.01 ± 0.05	2.57 ± 0.04	0.936 ± 0.005	0.68
A2063*	3.04	< 9.03	11.76 ± 0.02	3.39 ± 0.50	2.90 ± 0.44	0.974 ± 0.049	0.61
A2110	2.39	8.88 ± 0.16	11.91 ± 0.03	2.63 ± 0.38	1.52 ± 0.21	0.738 ± 0.021	1.00
A2199*	0.89	< 9.72	11.86 ± 0.02	3.25 ± 0.09	2.59 ± 0.06	0.940 ± 0.005	0.38
A2204*	5.69	< 9.77	12.15 ± 0.04	5.97 ± 0.25	7.34 ± 0.26	1.191 ± 0.009	1.00
A2355	4.75	10.29 ± 0.26	12.21 ± 0.05	6.17 ± 1.03	7.77 ± 1.11	1.135 ± 0.034	1.00
A2390*	6.89	< 12.05	12.33 ± 0.06	11.62 ± 0.97	22.9 ± 1.64	1.626 ± 0.024	0.89
A2415	4.79	11.13 ± 0.01	11.44 ± 0.02	2.18 ± 0.55	1.31 ± 0.28	0.731 ± 0.033	0.71
A2597*	2.49	< 10.65	11.57 ± 0.02	3.42 ± 0.14	2.83 ± 0.10	0.921 ± 0.007	0.54
A262	5.46	9.01 ± 0.08	11.63 ± 0.02	2.33 ± 0.08	2.06 ± 0.06	0.885 ± 0.008	0.34
A2626	4.33	9.71 ± 0.01	11.98 ± 0.03	3.20 ± 0.14	2.53 ± 0.10	0.911 ± 0.007	0.75
A2634	5.06	10.88 ± 0.15	11.77 ± 0.02	5.89 ± 0.32	7.19 ± 0.33	1.322 ± 0.013	0.50
A2665	6.04	8.58 ± 0.15	11.99 ± 0.03	2.68 ± 1.79	1.87 ± 1.07	0.822 ± 0.099	0.66
A2667	1.65	10.35 ± 0.27	11.97 ± 0.04	7.05 ± 1.09	9.77 ± 1.29	1.222 ± 0.034	1.00
A3017	2.09	9.76 ± 0.17	11.73 ± 0.02	4.71 ± 0.84	4.90 ± 0.75	0.983 ± 0.031	1.00
A3526*	8.1	< 10.55	11.77 ± 0.02	2.26 ± 0.01	1.40 ± 0.01	0.781 ± 0.001	0.82
A3528S*	6.13	< 8.77	12.11 ± 0.04	2.06 ± 0.24	1.19 ± 0.12	0.707 ± 0.015	0.88
A3581	4.25	10.41 ± 0.05	11.48 ± 0.01	1.62 ± 0.05	1.63 ± 0.03	0.814 ± 0.005	0.65
A3695	3.7	10.37 ± 0.08	11.90 ± 0.03	2.80 ± 0.29	2.01 ± 0.18	0.817 ± 0.015	1.00
A4059*	1.1	< 9.38	12.20 ± 0.04	5.96 ± 0.25	5.76 ± 0.34	1.208 ± 0.024	0.61
A478*	26.8	< 9.90	11.93 ± 0.03	7.82 ± 0.26	8.48 ± 0.93	1.327 ± 0.028	0.71
A496*	4.8	< 10.77	12.00 ± 0.03	7.51 ± 0.43	10.9 ± 0.53	1.513 ± 0.016	0.58
AS1101*	1.83	< 9.42	11.92 ± 0.03	1.37 ± 0.01	0.59 ± 0.01	0.560 ± 0.001	0.85
AS780	7.72	11.14 ± 0.01	12.25 ± 0.05	5.57 ± 0.68	6.52 ± 0.68	1.068 ± 0.023	1.00
AS851	4.96	9.76 ± 0.08	11.61 ± 0.02	0.73 ± 0.01	0.20 ± 0.01	0.412 ± 0.001	0.77

Table 2 continued

Table 2 (continued)

Hercules*	6.33	< 10.15	12.04 ± 0.03	3.25 ± 0.23	2.60 ± 0.16	0.840 ± 0.010	1.00
Hydra	4.84	10.99 ± 0.62	11.78 ± 0.02	4.13 ± 0.09	3.92 ± 0.07	1.054 ± 0.004	0.69
RXJ0058.9+2657	5.73	10.69 ± 0.08	11.91 ± 0.03	1.33 ± 0.07	0.57 ± 0.03	0.556 ± 0.006	0.79
RXJ0107.4+3227	5.41	9.88 ± 0.08	11.65 ± 0.02	6.07 ± 0.76	7.56 ± 0.81	1.361 ± 0.031	0.33
RXJ0123.6+3315	5.23	8.28 ± 0.01	11.69 ± 0.02	1.32 ± 0.03	0.56 ± 0.01	0.570 ± 0.002	0.26
RXJ0341.3+1524	16.17	9.53 ± 0.08	11.19 ± 0.02	1.72 ± 0.02	0.87 ± 0.01	0.656 ± 0.002	0.45
RXJ0352.9+1941	26.83	8.97 ± 0.06	11.85 ± 0.03	2.19 ± 0.15	1.96 ± 0.86	0.798 ± 0.019	0.75
RXJ0439.0+0520	10.3	11.95 ± 0.12	12.10 ± 0.04	3.19 ± 0.43	2.51 ± 0.29	0.770 ± 0.019	1.00
RXJ0751.3+5012*	5.09	< 9.21	11.33 ± 0.01	0.99 ± 0.07	0.34 ± 0.02	0.482 ± 0.006	0.40
RXJ0819.6+6336	4.16	8.47 ± 0.12	12.12 ± 0.04	3.55 ± 0.68	3.01 ± 0.50	0.911 ± 0.032	0.75
RXJ1050.4-1250	4.5	7.95 ± 0.09	11.39 ± 0.01	0.96 ± 0.06	0.33 ± 0.02	0.478 ± 0.005	0.53
RXJ1304.3-3031*	6.01	< 9.32	11.58 ± 0.02	0.95 ± 0.03	0.32 ± 0.01	0.477 ± 0.003	0.91
RXJ1315.4-1623	4.94	9.26 ± 0.08	11.44 ± 0.01	1.20 ± 0.03	1.43 ± 0.01	0.789 ± 0.003	0.30
RXJ1320.1+3308	1.05	9.32 ± 0.12	11.46 ± 0.01	1.04 ± 0.04	0.37 ± 0.01	0.487 ± 0.003	0.71
RXJ1501.1+0141	4.25	8.06 ± 0.08	11.21 ± 0.02	0.59 ± 0.09	1.22 ± 0.02	0.750 ± 0.004	0.23
RXJ1504.1-0248*	6.1	< 10.69	11.93 ± 0.03	6.99 ± 0.57	9.63 ± 0.67	1.233 ± 0.018	1.00
RXJ1506.4+0136	4.24	8.97 ± 0.23	11.31 ± 0.01	0.89 ± 0.01	0.28 ± 0.01	0.460 ± 0.001	0.47
RXJ1522.0+0741*	3.05	< 8.91	11.63 ± 0.02	2.96 ± 0.10	2.22 ± 0.06	0.880 ± 0.005	0.65
RXJ1524.2-3154*	8.44	< 10.55	11.87 ± 0.03	3.00 ± 0.21	2.26 ± 0.13	0.841 ± 0.010	0.70
RXJ1539.5-8335	7.68	10.19 ± 0.15	12.10 ± 0.04	1.76 ± 0.28	0.91 ± 0.1	0.635 ± 0.018	0.67
RXJ1558.4-1410	11.47	12.23 ± 0.15	12.19 ± 0.04	3.84 ± 0.22	3.45 ± 0.17	0.972 ± 0.010	0.64
RXJ1604.9+2356	4.99	10.77 ± 0.06	11.85 ± 0.02	2.27 ± 0.28	1.41 ± 0.15	0.766 ± 0.017	0.53
RXJ1715.3+5725	2.6	9.96 ± 0.55	11.75 ± 0.02	1.37 ± 0.02	0.59 ± 0.01	0.575 ± 0.001	0.39
RXJ1720.1+2638*	3.89	< 9.15	12.13 ± 0.04	5.39 ± 0.46	6.17 ± 0.45	1.115 ± 0.017	1.00
RXJ1750.2+3504	3.12	11.08 ± 0.15	12.17 ± 0.04	3.00 ± 0.49	2.27 ± 0.31	0.791 ± 0.023	1.00
RXJ1844.1+4533	6.32	10.72 ± 0.01	11.97 ± 0.03	1.72 ± 0.11	0.88 ± 0.01	0.618 ± 0.007	1.00
RXJ2129.6+0005*	4.16	< 9.76	12.16 ± 0.04	4.30 ± 0.36	4.19 ± 0.3	0.921 ± 0.014	1.00
Z1665*	2.74	< 9.09	11.65 ± 0.02	1.48 ± 0.26	0.68 ± 0.1	0.601 ± 0.019	0.56
Z235*	3.91	< 10.65	11.95 ± 0.03	3.45 ± 0.35	2.87 ± 0.25	0.926 ± 0.017	0.55
Z3146*	2.93	< 8.73	12.19 ± 0.06	5.59 ± 0.55	6.57 ± 0.55	1.024 ± 0.018	1.00
Z7160*	3.22	< 9.03	12.41 ± 0.06	3.60 ± 0.26	3.09 ± 0.19	0.817 ± 0.011	1.00
Z808*	7.55	< 9.06	11.95 ± 0.03	3.03 ± 0.58	2.30 ± 0.38	0.797 ± 0.027	1.00
Z8193*	2.31	< 11.33	12.28 ± 0.05	4.47 ± 0.71	4.47 ± 0.61	0.989 ± 0.028	0.72
Z8276	3.66	10.53 ± 0.54	11.89 ± 0.03	3.79 ± 0.23	3.38 ± 0.17	0.985 ± 0.011	0.94

*Sources where the BH mass is an upper limit

NOTE—Columns are as follows: (1) Name of the galaxy cluster; (2) Line-of-sight column density to the cluster (Kalberla et al. 2005); (3) BH mass obtained from the Fundamental Plane relation (Merloni et al. 2003); (4) Stellar bulge mass of the BCG calculated using K-band luminosity and the mass-to-light ratio of 0.85 (Bell et al. 2003); (5) Best-fit temperature of the ICM; (6) M_{500} mass inferred from the best-fit temperature in column (5) using the $kT - M_{500}$ relation of Lovisari et al. (2015); (7) R_{500} radius of the cluster; (8) The fraction of the R_{500} radius included in the *Chandra* field of view. The errors associated with the M_{500} mass and R_{500} radius were computed from the temperature uncertainties.

To accurately measure the ICM temperature, we first identified the peak of the X-ray emission, which is considered to be the center of the cluster. To find the X-ray

3.1.2. Measuring the Temperature of the ICM

peak, we smoothed the 0.7 – 2 keV band images with a Gaussian with a kernel size of 3. We searched for the maximum on this smoothed image, which defined the peak of the emission. We note that the center of the cluster may be slightly offset from the BCG (Hudson et al. 2010). Several clusters in our sample exhibit double peaked profiles, as these may be undergo mergers (see Section 5). In these cases the second peak was masked from the observations.

After we identified the center of each cluster, we determined the R_{500} radius. As the first step, we computed the signal-to-noise ratio in the 0.7 – 2 keV band using concentric annuli. The first spectra were extracted within a radius where the signal-to-noise ratio peaked. After extracting the spectrum, we determined the initial temperature and an initial M_{500} ¹ using the $kT - M_{500}$ relation by Lovisari et al. (2015):

$$\log_{10} \left(\frac{M_{500}}{5 \times 10^{13} h^{-1} M_{\odot}} \right) = 1.71 \log_{10} \left(\frac{kT}{2 \text{ keV}} \right) + 0.20 \quad (1)$$

Where h is the reduced Hubble constant. This M_{500} value was then used to calculate the R_{500} radius.

Once the initial R_{500} radius was retrieved, we followed the iterative process outlined in Lovisari et al. (2017) to measure the gas temperature of the ICM. Specifically, we extracted the source and background spectra from the $(0.15 - 0.75)R_{500}$ region, in order to exclude the central regions where there could be an extreme temperature gradient. These spectra were fit using *XSpec* (Arnaud 1996). From the fit we obtained a new temperature, and, hence M_{500} value using the $kT - M_{500}$ relation in Lovisari et al. (2015). This new M_{500} and the inferred R_{500} defined the new extraction annulus. We continued to iterate via this process until the temperature remained invariant within 5%. Although Lovisari et al. (2017) used the $M - Y_x$ relation, in this work we rely on the $kT - M_{500}$ relation for consistency with Bogdán et al. (2018). For most of the clusters, the extraction region lay within the field-of-view of the analyzed *Chandra* observations. However, for a small sample of nearby clusters, only a relatively small fraction of the R_{500} were included in the field-of-view. For these systems, we utilized multiple observations to increase the coverage of the clusters. In Appendix A we show all the *Chandra* images of the clusters in the 0.7–2.0 keV band as well as the annulus which the final spectra was extracted from defined by the R_{500} value.

¹ M_{500} is the mass contained within the radius where the density of the cluster is 500 times the critical density of the Universe

Spectra along with the corresponding response files for the source and background data were extracted using the *spectextract* and *dmextract* tools, respectively. The background spectra were renormalized using the count rate ratios observed in the 10 – 12 keV band, and the renormalized background spectrum was subtracted from the source spectrum. The background-subtracted source spectrum was grouped by count number with each bin requiring a minimum of 15 counts. This final spectrum was used to fit a model and determine the ICM temperature of the galaxy cluster.

We used the spectral analysis software, *XSpec*, to fit a model to the data (Arnaud 1996). Fitting was performed in the 0.7 – 5 keV energy band. We fit the emission with an *apec* model that describes collisionally ionized thermal plasma. We allowed the abundance, temperature and normalization to vary. For the abundances we used the table of Anders & Grevesse (1989) In addition, we included photoelectric absorption, whose value were the weighted average from the Leiden/Argentine/Bonn (LAB) survey (Kalberla et al. 2005). This procedure resulted in acceptable fits for most clusters in our sample. However, for two clusters, A478 and J0352.9+1941, the column densities provided by the LAB survey were underestimated. We obtained significant residuals at < 1 keV for the spectra of these clusters. The LAB survey underestimates column densities, and this underestimation becomes strongly significant for high values (excess of 10^{21}), such as for these clusters. Therefore, for these two systems we allowed the column density to vary during the fitting process. Allowing this parameter to vary results in an acceptable fit.

In Table 2 we list the obtained R_{500} and M_{500} values as well as the best-fit ICM temperatures.

3.2. Cool Core and Non-Cool Core Clusters

Given our larger sample size, we aim to explore whether the $M_{\text{BH}} - kT$ relationship exhibits variations for different types of clusters. Specifically, we split our sample into cool core (CC) and non-cool core (NCC) clusters. Due to their dynamics, CC clusters generally have greater gas inflow to the center (Hudson et al. 2010). This process may increase the growth rate of the BH residing in the BCG. This, in turn, could lead to differences in the $M_{\text{BH}} - kT$ relation for CC and NCC clusters.

There are several parameters that can be used to distinguish between these two types of cluster and the debate is ongoing as to which parameter is the most accurate. Therefore, we used four parameters to split the galaxy cluster samples into CC and NCC clusters to ex-

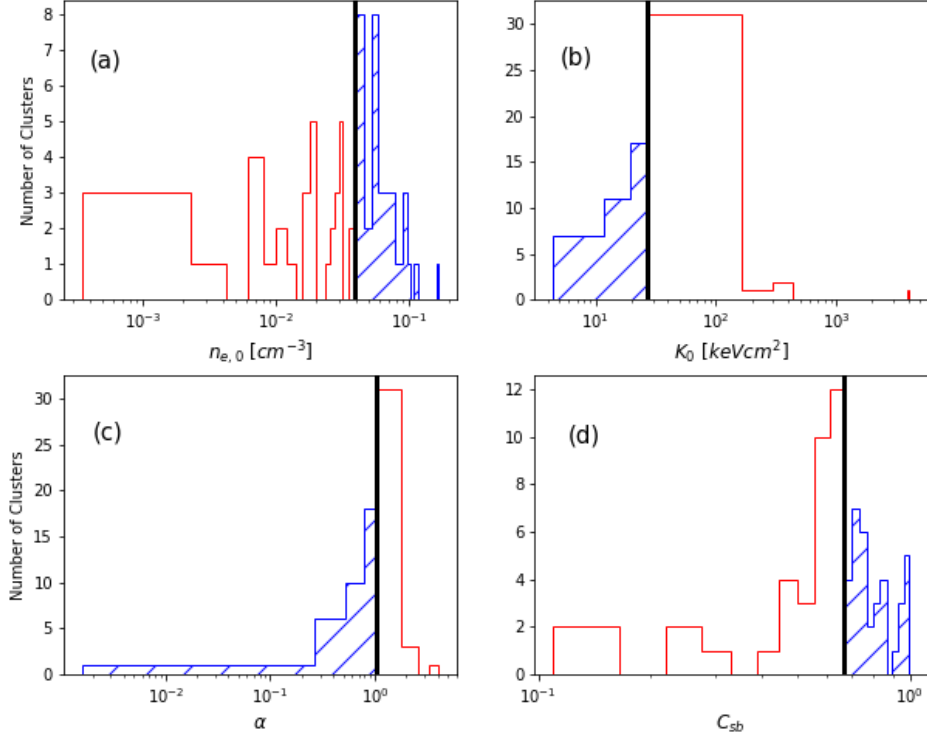


Figure 2. The distributions of relaxed and disturbed clusters based on the four parameters from Hudson et al. (2010); (a) central electron density, $n_{e,0}$, (b) central entropy, K_0 , (c) cuspsiness, α , and (d) central surface brightness, C_{sb} . The relaxed clusters, which have similar properties to CCs are shown in blue hatch. The disturbed clusters, which can be likened to NCC clusters, are shown in red. The black lines indicate the median for each parameter where the clusters split into the two subsamples.

amine whether there is a difference in the $M_{\text{BH}}-kT$ relationship. These parameters are central electron density, central entropy, cuspsiness, and surface brightness density (Hudson et al. 2010). Instead of using a value from literature, the median value of each of the parameters was used to split our sample. We split our clusters in this way because, if we were to use a value from the literature, then we would need our data to be calibrated perfectly with the original work. As this is difficult, by using the median value instead of classifying the clusters definitively as a CC (NCC), we simply make a distinction between more relaxed (disturbed) systems. Therefore from now on we will refer to the two populations as more relaxed, e.g. clusters showing CC properties, and more disturbed (clusters showing NCC properties).

To calculate these parameters, we constructed surface brightness profiles in the 0.7–2 keV band for each cluster. For each cluster, we created 38 concentric annuli with a minimum of 10 pixels and a maximum of 200 pixels. To account for the background, we used the blank-sky images in the same energy range and with the same annuli. The obtained background subtracted surface brightness profiles were fit with a double-beta

model (Hudson et al. 2010):

$$\Sigma = A_{0,1} \left[1 + \left(\frac{r}{r_{c,1}} \right)^2 \right]^{-3\beta_1 + 0.5} + A_{0,2} \left[1 + \left(\frac{r}{r_{c,2}} \right)^2 \right]^{-3\beta_2 + 0.5} \quad (2)$$

where $A_{0,1}$ and $A_{0,2}$ are the amplitudes, $r_{c,1}$ and $r_{c,2}$ are the core radii. The values for amplitude, core radii and $\beta_{1,2}$ were fit for each cluster. Based on these, we computed the four parameters to define the relaxed and disturbed cluster sub-samples. The obtained distribution of these sub-samples are shown in Figure 2.

3.2.1. Central Electron Density

To calculate the central electron density ($n_{e,0}$) from the double-beta model, we use:

$$n_{e,0} = \left[n_{e,1}^2 \left(1 + \left(\frac{r}{r_{c,1}} \right)^2 \right)^{-3\beta_1} + n_{e,2}^2 \left(1 + \left(\frac{r}{r_{c,2}} \right)^2 \right)^{-3\beta_2} \right]^{\frac{1}{2}} \quad (3)$$

where $n_{e,1}$ and $n_{e,2}$ are the central electron densities for each component in the double-beta model. The calculation of these quantities depends upon n_0 , i.e. the central density:

$$n_0 = \left(\frac{10^{14} 4\pi D_A D_L \zeta N}{EI} \right)^{0.5} \quad (4)$$

where N is the normalization obtained from the best-fit *apev* model. To calculate the value of n_0 , we used

$0.048R_{500}$ as the central extraction region (Hudson et al. 2010). The electron densities $n_{e,1}$ and $n_{e,2}$ for the double-beta model were calculated following Hudson et al. (2010).

The value of $n_{e,0}$ could be used to classify clusters as either disturbed or relaxed. The median which we took as a “splitting” value was $n_{e,0} = 0.040 \text{ cm}^{-3}$. Clusters with a density less than this value were classified as disturbed systems, as a hotter central temperature indicates a lower central density which is characteristic of a NCC system.

3.2.2. Central Entropy

To split the clusters based on their central entropy (K_0), we compute this parameter using:

$$K_0 = k_B T_0 n_{e,0}^{-\frac{2}{3}} \quad (5)$$

where T_0 is the central temperature, which is computed for the $0.048R_{500}$ region, thereby maintaining consistency with the normalization in Equation 4. The “splitting” value for this parameter is $K_0 = 26.59 \text{ keV cm}^2$. If K_0 was less than this value then the cluster would be classified as a relaxed cluster as the gas at the center is cooler and hence less perturbed.

3.2.3. Cuspiness

The cuspiness parameter (α) was suggested as a parameter for identifying CC clusters at large redshifts (Vikhlinin et al. 2007) and it is defined as:

$$\alpha = -\frac{d \log(n_e(r))}{d \log(r)} \quad (6)$$

when $r = 0.04R_{500}$. As our density function is based on the double-beta model we can recast Equation 6 as the following:

$$\alpha = 3r^2 \frac{\Sigma_{12} L I_2 \beta_1 r_{c,1}^{-2} b'_1 + L I_1 \beta_2 r_{c,2}^{-2} b'_2}{\Sigma_{12} L I_2 b_1 + L I_1 b_2} \quad (7)$$

where the core radii and the $\beta_{1,2}$ are the values found from fitting the double-beta model (Equation 2) to the surface brightness profile. The values $L I_i$ are the line emission measure for model i and σ_{12} is the ratio of the central surface brightness of model 1 to model 2. Finally, b_i, b'_i are defined as:

$$b_i = \left(1 + \left(\frac{r}{r_{c,i}}\right)^2\right)^{-3\beta_i} \quad (8)$$

and

$$b'_i = \left(1 + \left(\frac{r}{r_{c,i}}\right)^2\right)^{-3\beta_i - 1} \quad (9)$$

where $i=1,2$. For further details we refer to Hudson et al. (2010).

The median “splitting” value for this parameter is $\alpha = 1.05$. If $\alpha > 1.05$ then the cluster is classified as disturbed.

3.2.4. Surface Brightness Density

The final parameter we used to identify clusters as either CC or NCC was the surface brightness density, C_{sb} . This parameter was first used by Santos et al. (2008), as a way to measure the excess of brightness at the core of a cluster. The C_{sb} is defined as:

$$C_{sb} = \frac{\Sigma(r < 40\text{kpc})}{\Sigma(r < 400\text{kpc})} \quad (10)$$

In other words, the C_{sb} is the ratio of the integrated surface brightness within a radius 40 kpc to that within a radius of 400 kpc. For this parameter a median “splitting” value of $C_{sb} = 0.66$ is used where clusters with a C_{sb} greater than this value are classified as relaxed clusters, as CC clusters are bright at the center (Fabian et al. 1984).

We note that the median values we use to split the samples into relaxed and disturbed clusters differ from the literature, but this is to be expected due to differences between our samples and the data used.

4. RESULTS

4.1. Correlations

In the top left and right panels of Figure 3, we depict the observed relation between the BH mass and the cluster temperature and stellar bulge mass, respectively. Note that the BH masses are inferred from the Fundamental Plane relation (Merloni et al. 2003). The errors in the BH masses were calculated using the uncertainties obtained for the X-ray and radio luminosities of the BHs. To infer the BH mass from the Fundamental Plane, it is necessary to detect the BHs both in radio and X-ray wavelengths. However, in the sample of Mezcua et al. (2018) several BHs remain undetected in the X-ray band. Therefore, for these BHs we compute upper limits on the BH mass. To derive the stellar mass of the BCGs, we rely on Mezcua et al. (2018), who provides the K-band absolute magnitude of the galaxies. We convert the K-band luminosities to stellar mass using the K-band mass-to-light ratio of 0.85, which is typical for massive elliptical galaxies (Bell et al. 2003). On the plots we add the data points from Bogdán et al. (2018), which used nearby galaxy groups/clusters with dynamically measured BHs. In the bottom left and right panels of Figure 3, we show the relations between the inferred BH mass against cluster mass inferred from the $kT - M_{500}$ relation (Lovisari et al. 2015), as well as the relation between bulge mass and best-fit cluster temperature, respectively. We note that for six clusters in our

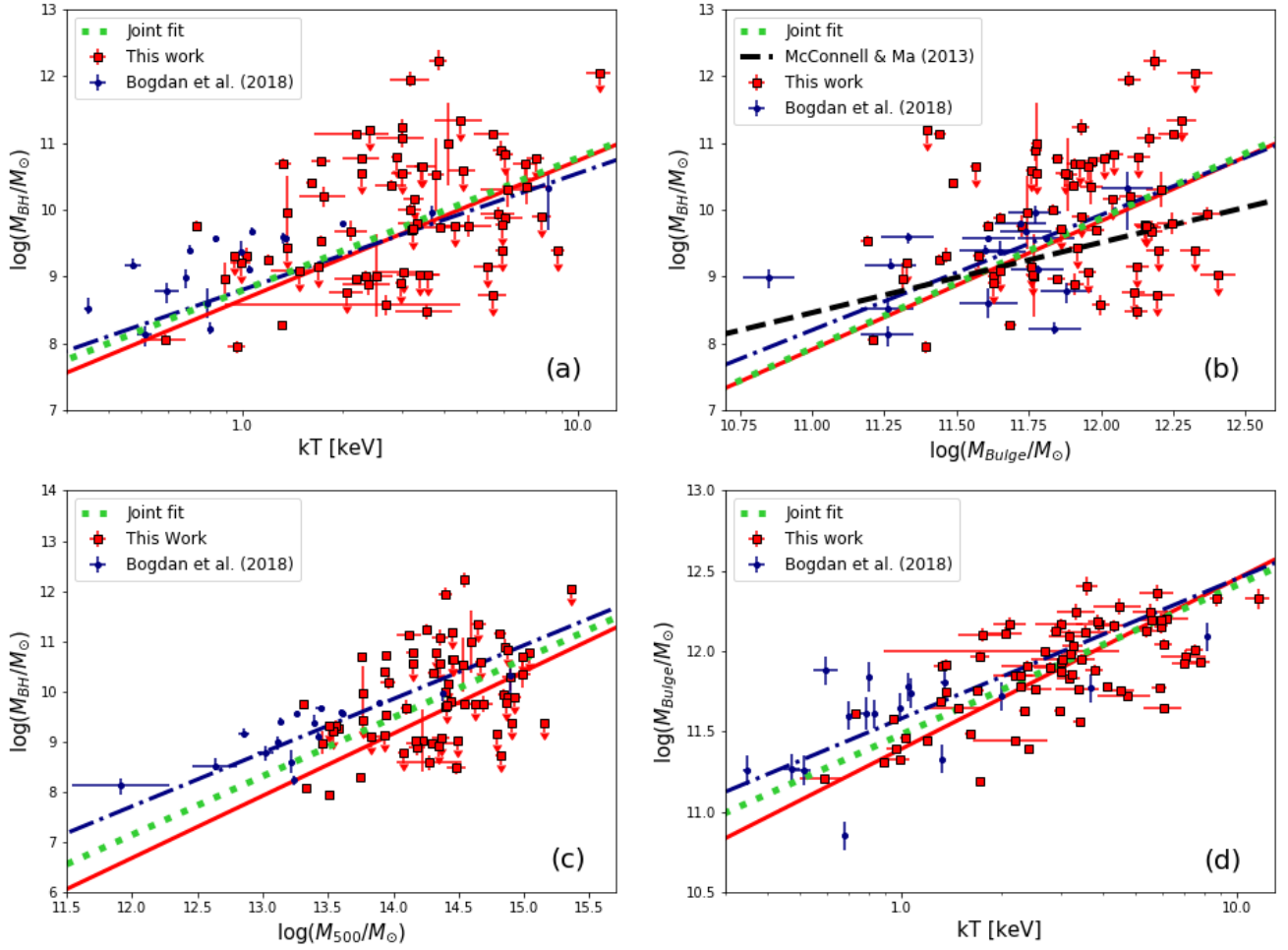


Figure 3. Scaling relations investigated in this paper: (a) BH mass – cluster temperature relation, (b) BH mass – bulge mass relation, (c) BH mass – cluster mass relation, and (d) bulge mass – cluster temperature relation. The red squares are from this work with downward arrows indicating upper limits in BH mass. The blue circles are for the BGGs/BCGs studied in [Bogdán et al. \(2018\)](#). The best-fitting lines for the data is shown with the solid line and were all calculated with BCES_REGRESS code. For the fitting procedure the upper limits were included. The dot-dashed line in the relation from [Bogdán et al. \(2018\)](#), the dotted line is from a joint fit based on the sample of this work and [Bogdán et al. \(2018\)](#) data, and in panel (b) the dashed line is the $M_{\text{BH}} - M_{\text{bulge}}$ relation from [McConnell & Ma \(2013\)](#).

Table 3. Best-fit parameters on linear regression for our data

Relation	α	β	$\sigma_{\text{intrinsic}}^x$	$\sigma_{\text{intrinsic}}^y$	r^*	ρ^{**}
$M_{\text{BH}} - kT$	-0.35 ± 0.21	2.08 ± 0.43	0.35	0.91	0.26	0.24
$M_{\text{BH}} - M_{\text{bulge}}$	-1.09 ± 0.39	1.92 ± 0.45	0.49	0.96	0.26	0.24
$M_{\text{BH}} - M_{500}$	-1.08 ± 0.25	1.24 ± 0.19	0.69	0.99	0.18	0.20
$M_{\text{Bulge}} - kT$	0.39 ± 0.05	1.06 ± 0.08	0.23	0.22	0.66	0.62

* Pearson Correlation Coefficient

** Spearman Correlation Coefficient

sample, the fraction of the R_{500} radius covered by the field of view of *Chandra* is $R_{\text{frac}} < 0.4$. After examining these clusters, we concluded that the BHs associated with their BCGs are not preferentially over-massive or under-massive relative to other systems. As such, these data points do not introduce a bias in our results.

To compute the best-fit relations, we used the BCES_REGRESS code (Akritas & Bershady 1996). This linear regression code uses bivariate correlated errors and intrinsic scatter fitting method. It is advantageous to use this over standard linear regression fitting as it allows for the errors in both the x and y measurements to be taken into account. We performed the fits in log – log space and used the *bisector* method. In order to perform a fitting that included the upper limited sources we adopted the following method. For the non detections (shown with arrows in Figure 3), we calculated a lower limit on the BH mass and then assumed that the true BH mass could be represented by a random uniform distribution between the upper and lower limits. The lower limits were calculated using the $M_{\text{BH}} - M_{\text{bulge}}$ relation of McConnell & Ma (2013). We take the lower limits to be 3σ below the predicted value from this relation. In order to implement the BCES_REGRESS code, all variables need an error. Therefore the non detections, for the BH masses we assume that the errors are 25% of the range between the measured upper limit and the calculated lower limit. We tested different percentages for the errors but found no significant difference in the result. For the detected BH mass points, we assumed a Gaussian distribution between the error range centered on the measured value. With these two random distributions for the detections and non detections we implemented the fitting code via a Monte Carlo simulation and repeated 10^4 times. The values quoted below and in Table 3 are the mean from all these realizations. We obtained the following relationships:

$$\log_{10} \left(\frac{M_{\text{BH}}}{10^9 M_{\odot}} \right) = -0.35 + 2.08 \log_{10} \left(\frac{kT}{1 \text{ keV}} \right) \quad (11)$$

$$\log_{10} \left(\frac{M_{\text{BH}}}{10^9 M_{\odot}} \right) = -1.09 + 1.92 \log_{10} \left(\frac{M_{\text{bulge}}}{10^{11} M_{\odot}} \right) \quad (12)$$

$$\log_{10} \left(\frac{M_{\text{BH}}}{10^9 M_{\odot}} \right) = -1.08 + 1.45 \log_{10} \left(\frac{M_{500}}{10^{13} M_{\odot}} \right) \quad (13)$$

$$\log_{10} \left(\frac{M_{\text{Bulge}}}{10^{11} M_{\odot}} \right) = 0.39 + 1.06 \log_{10} \left(\frac{kT}{1 \text{ keV}} \right) \quad (14)$$

The intrinsic scatter in both the x and y planes were calculated following Lovisari et al. (2015):

$$\begin{aligned} \sigma_{\text{intrin}}^y &= \sqrt{(\sigma_{\text{tot}}^y)^2 - (\sigma_{\text{stat}}^y)^2 - (a^2(\sigma_{\text{stat}}^x)^2)} \\ \sigma_{\text{intrin}}^x &= \sqrt{(\sigma_{\text{tot}}^x)^2 - (\sigma_{\text{stat}}^x)^2 - (a^{-2}(\sigma_{\text{stat}}^y)^2)} \end{aligned} \quad (15)$$

Where $\sigma_{\text{tot}}^{x,y}$ and $\sigma_{\text{stat}}^{x,y}$ represent the total and statistical scatter along x and y, and the value, a , is the gradient calculated from the BCES_REGRESS code. The best-fit relations, the scatter, and the Pearson and Spearman correlation coefficients are tabulated in Table 3.

The best-fit $M_{\text{BH}} - kT$ relation is somewhat steeper and exhibits larger scatter than the relation found in Bogdán et al. (2018). We note that the bulge masses in this work and in that of Bogdán et al. (2018) were calculated using different methods. To make the $M_{\text{BH}} - M_{\text{bulge}}$ relations comparable, we re-computed the bulge masses for the sample of Bogdán et al. (2018) using the method applied in this work. The $M_{\text{BH}} - M_{\text{bulge}}$ relations are identical within 1σ uncertainties. The intrinsic scatter in the $M_{\text{BH}} - kT$ and $M_{\text{BH}} - M_{\text{bulge}}$ relations are $\sigma_{\text{intrin}}^y = 0.91$ and 0.96 respectively, which exceeds those found in Bogdán et al. (2018) and is comparable with the scatter in the Fundamental Plane relation of 0.88 found by Merloni et al. (2003).

In the bottom left panel of Figure 3 we plot the BH mass against the M_{500} mass of each cluster. To convert the cluster temperature to M_{500} , we used the $kT - M_{500}$ relation of Lovisari et al. (2015) (Equation 1). The $M_{\text{BH}} - M_{500}$ relationship (Equation 13) is consistent to within 1σ with that found by Bogdán et al. (2018). In the bottom right panel of Figure 3, we show the relation between the stellar bulge mass and the cluster temperature. While this relation exhibits smaller scatter (see Table 3), the best-fit relation and the correlation coefficients are comparable to that obtained in Bogdán et al. (2018).

4.2. Joint Fit Correlations

The sample investigated in this work explores the high-mass end of the relations, while Bogdán et al. (2018) studied the low-mass end of the scaling relations. Therefore, here, we combine the two samples and perform joint fitting to establish relations, which are constrained across a broad range of galaxy groups and clusters with temperatures of $kT = 0.4 - 12$ keV. We find the best-fitting equations to be:

$$\log_{10} \left(\frac{M_{\text{BH}}}{10^9 M_{\odot}} \right) = -0.21 + 1.98 \log_{10} \left(\frac{kT}{1 \text{ keV}} \right) \quad (16)$$

$$\log_{10} \left(\frac{M_{\text{BH}}}{10^9 M_{\odot}} \right) = -1.07 + 1.94 \log_{10} \left(\frac{M_{\text{bulge}}}{10^{11} M_{\odot}} \right) \quad (17)$$

Table 4. Best-fit parameters on linear regression for joint fitting

Relation	α	β	$\sigma_{intrinsic}^x$	$\sigma_{intrinsic}^y$	r^*	ρ^{**}
$M_{BH} - kT$	-0.21 ± 0.10	1.98 ± 0.24	0.35	0.84	0.37	0.35
$M_{BH} - M_{bulge}$	-1.07 ± 0.26	1.94 ± 0.32	0.53	0.96	0.31	0.28
$M_{BH} - M_{500}$	-0.82 ± 0.12	1.16 ± 0.10	0.72	0.92	0.31	0.31
$M_{Bulge} - kT$	0.48 ± 0.04	0.93 ± 0.07	0.23	0.25	0.70	0.69

*Pearson Correlation Coefficient

**Spearman Correlation Coefficient

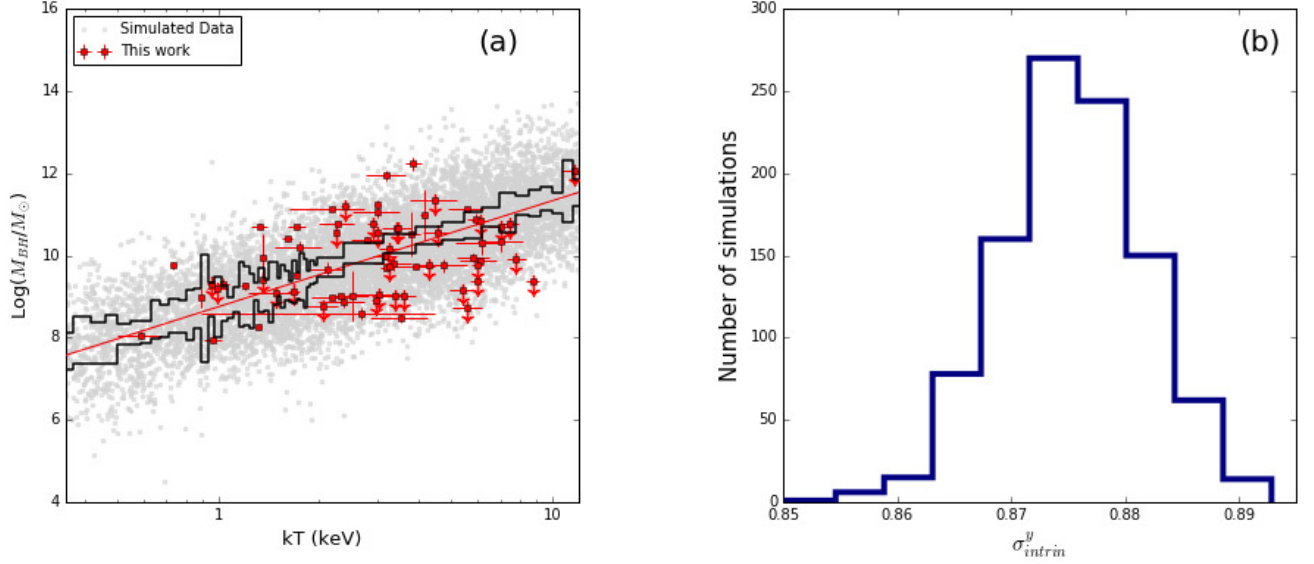


Figure 4. Panel (a) shows the relationship between BH mass and cluster temperature. The red squares are the results from this work, downward arrows indicate upper limits. The light grey circles – or cloud of data – are the simulated data points from the Monte Carlo program. The red solid line is the relation from Equation 11 calculated using BCES.REGRESS code. The black lines either side the red one is the 1σ contours from the line of best fit for the simulated data. Panel (b) shows the distribution in $\sigma_{intrinsic}^y$ for the 1000 simulations.

$$\log_{10} \left(\frac{M_{BH}}{10^9 M_{\odot}} \right) = -0.82 + 1.16 \log_{10} \left(\frac{M_{500}}{10^{13} M_{\odot}} \right) \quad (18)$$

$$\log_{10} \left(\frac{M_{Bulge}}{10^{11} M_{\odot}} \right) = 0.48 + 0.92 \log_{10} \left(\frac{kT}{1 \text{ keV}} \right) \quad (19)$$

The intrinsic scatter in both axis was also calculated for the joint sample using Equation 15, as well as the Pearson and Spearman correlation coefficients. All results are summarized in Table 4. The joint fit relations are visualized in Figure 3 as the dotted green line. From Table 4, it is clear that the $M_{BH} - kT$ relation is slightly tighter than the $M_{BH} - M_{bulge}$ relation. This is likely due to the relation for the joint fit being driven by the dynamically measured BHs. The scatter in both the $M_{BH} - kT$ and the $M_{BH} - M_{bulge}$ relation has been reduced, however the scatter arising from the Fundamental Plane relation likely plays a notable role.

4.3. Monte Carlo simulations

Given that the scatter in the $M_{BH} - kT$ and the Fundamental Plane relation are comparable, we investigate whether the intrinsic scatter of the Fundamental Plane relation may be responsible for the observed scatter in the $M_{BH} - kT$ relation. Therefore, we performed Monte Carlo simulations.

We assumed that the relation in Equation 11 was perfect and used it to determine the masses of BHs using a random distribution of 10^4 temperatures within the temperature range of our data. A Gaussian distribution was created using a scatter of 0.88 that characterizes the Fundamental Plane relationship of Merloni et al. (2003), which was convolved with the BH masses produced to give a randomly scattered sample of simulated data. We then calculated the best-fit relation using BCES.REGRESS code and the intrinsic scatter in the y-direction ($\sigma_{intrinsic}^y$) for the simulated data. We repeated

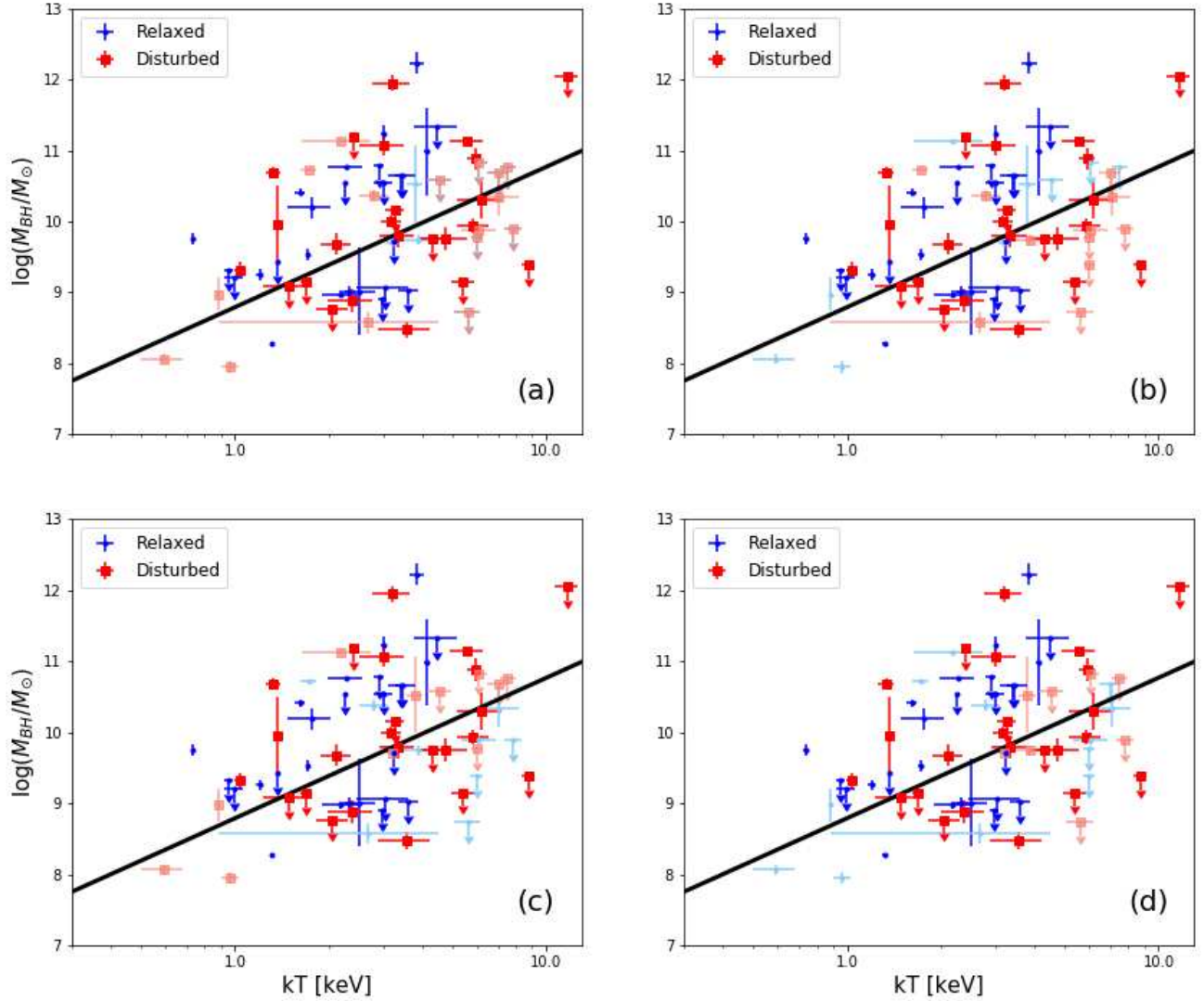


Figure 5. Plot of BH mass against cluster temperature for each of the four parameters used to distinguish between relaxed and disturbed systems; (a) Central Electron Density, (b) Central Entropy, (c) Cuspidity and (d) Concentrated Surface Brightness. The blue circles and red squares indicate relaxed and disturbed clusters respectively where points represented with arrows are upper limits. Darker colours indicate sources which were identified as either CC-like or NCC-like by more than three parameters. The solid line represents the best-fit $M_{\text{BH}} - kT$ relation obtained for the full joint sample (Equation 16).

this 10^3 times, and derived the gradient, y-intercept, and $\sigma_{\text{intrinsic}}^y$ for each realization.

The left panel of Figure 4 shows one representative realization of the simulation along with the observed data for the $M_{\text{BH}} - kT$ relationship. All the observed points lie within the range set by the simulated data, hinting that at least part of the scatter in our data may be due to the Fundamental Plane relation.

In the right panel of Figure 4 we show the distribution of $\sigma_{\text{intrinsic}}^y$ for the simulations. We find that 68% of the simulation have a scatter in the range of $\sigma_{\text{intrinsic}}^y = 0.87 - 0.89$, which is similar to the scatter of the Fundamental Plane relation. We find that the observed scatter of $\sigma_{\text{intrinsic}}^y = 0.91$ is observed in none of the re-

alizations. It is possible that dominant fraction of the scatter is introduced due to the Fundamental Plane relation that was used to infer the BH masses but further factors may also contribute to the scatter. These are further discussed in Section 5.

4.4. Investigating cool core and non-cool core clusters

In Section 3.2, we used the median of each morphological parameter to split the sample into the most relaxed (CC like) and most disturbed (NCC like) systems.

In Figure 5 we plot the BH mass against cluster temperature for each of the four parameters to probe if there is any distinction between the two types. We find that relaxed and disturbed clusters do not occupy different

parts of the parameter space. This hints that BHs do not undergo drastically different evolution in the centers of these two categories of cluster. Therefore although galaxy/cluster mergers and cooling flows could be contributing to the unexpected growth of the BH in the BCG, we cannot identify the most significant cause. To further investigate the relations, we make a distinction between clusters for which three or more parameters identified them as relaxed or disturbed. However, we do not find statistically significant differences between the two populations. We implemented the same fitting method as in 4.1 using the BCES_REGRESS code for each of the parameters. We found that for each parameter, the difference in the $M_{\text{BH}} - kT$ relation for the two sub-samples was statistically insignificant, therefore we still cannot justify the cause of the unexpected growth for clusters that resemble properties similar to CC and NCC systems.

5. DISCUSSION

5.1. Tightness of the scaling relations

In this work, we investigated the tightness of the relations between the total mass of galaxy clusters (traced by the best-fit gas temperature), the stellar mass of BCGs, and the mass of the central BH.

We found that the best-fit $M_{\text{BH}} - kT$ relation is similar to that found by Bogdán et al. (2018), albeit the scatter is significantly larger (Table 3). While the dominant fraction of the scatter likely originates from the intrinsic scatter in the fundamental plane relation, part of the scatter in the relation may arise from uncertainties in measuring the X-ray and radio luminosity of the BH as well as measuring the cluster temperature. Specifically, resolving the nuclear X-ray source and deriving its luminosity is challenging in the center of luminous galaxy clusters (Mezcua et al. 2018). In a fraction of the BCG sample, the BHs remained undetected, which might be either due to the dormant nature of the BHs or the luminous ICM in which the BCG is embedded. Thus, the large observed scatter in the $M_{\text{BH}} - kT$ relation is likely due to the combination of the intrinsic scatter of the Fundamental Plane relation, measurement uncertainties in the X-ray luminosity of the BH and ICM temperature, and the intrinsic scatter in the relation.

The scatter in the $M_{\text{BH}} - M_{\text{bulge}}$ relation is comparable to that obtained for the $M_{\text{BH}} - kT$ relation. Because the scatter for both relations is dominated by the intrinsic scatter of the Fundamental Plane, our results do not contradict Bogdán et al. (2018), who found lower scatter and tighter correlation for the $M_{\text{BH}} - kT$ relation. This result is further supported by the joint fitting of this and Bogdán et al. (2018) data sets. Again the $M_{\text{BH}} -$

kT relation is tighter than the $M_{\text{BH}} - M_{\text{bulge}}$, but both exhibit similar scatter.

The discrepancies in the $M_{\text{BH}} - kT$ relation between our work and that of Bogdán et al. (2018) are likely due to the different populations of galaxy groups and clusters. The sample of Bogdán et al. (2018) was mainly dominated by galaxy groups, and their sample included only two systems with an ICM temperature greater than 2 keV. This implies that their relation in the high mass end is not well constrained. In this work, we mainly study massive galaxy clusters. Indeed this sample consists of 53 clusters with a temperature greater than 2 keV. Therefore the nature of the $M_{\text{BH}} - kT$ relationship is dictated largely by the high mass clusters resulting in a steeper relation.

Our results suggest that the $M_{\text{bulge}} - kT$ is the tightest relationship (Table 3). The scatter and the tightness of this relation is comparable with that obtained in Bogdán et al. (2018). However, we note that both M_{bulge} and kT are directly measured quantities, unlike those where the M_{BH} is inferred from the Fundamental Plane. Therefore, it is not surprising that there is less scatter observed in this relationship. From the joint fitting, we can draw a similar conclusion.

Hence, the observed scaling relations are not inconsistent with the results of Bogdán et al. (2018). However, to conclusively confirm that the $M_{\text{BH}} - kT$ relation is tighter than the $M_{\text{BH}} - M_{\text{bulge}}$ relation, more accurate BH mass measurements would be required.

5.2. Processes aiding the growth of BHs in BCGs

Our results demonstrate that for a given stellar bulge mass, BCGs have more massive BHs than satellite galaxies. This can be seen in panel (b) of Figure 3 where we have plotted BH mass against BCG stellar mass. On this plot we added the $M_{\text{BH}} - M_{\text{bulge}}$ relation of McConnell & Ma (2013) to emphasize how overly massive most of these particular BHs are. It is worth noting that the best-fit $M_{\text{BH}} - M_{\text{bulge}}$ relation presented in McConnell & Ma (2013) (see Figure 3) includes BCGs. Excluding BCGs would result in a shallower $M_{\text{BH}} - M_{\text{bulge}}$ relation, implying that the BHs studied in this work would be even stronger outliers. Therefore, we overview the physical processes that may aid the growth of these BHs.

A candidate process that could be contributing to the accelerated growth of BHs in BCGs is galaxy-galaxy mergers. Mergers play an important role in the growth of BCGs since BCGs grow a factor of 1.8 in mass between $z=1$ and the present-day universe (Burke & Collins 2013). At the centers of galaxy clusters, mergers are more frequent than in field or satellite galaxies. Clusters with similar total mass can exhibit different BCG

merging histories. Within 50 kpc radius a BCG can have on average ~ 6.45 companions, which over time will in-fall and merge with the BCG (Burke & Collins 2013). A merger of a gas-rich galaxy could directly feed the BH and induce star formation, hence the $M_{\text{BH}} - M_{\text{bulge}}$ relation may still hold. However, Kaviraj (2014) suggested that certain merger events weaken the coupling between stellar mass and BH growth which would allow for a larger scatter in this relationship, especially for BCGs.

Structure formation simulations established that BHs with masses $> 10^9 M_{\odot}$ predominantly grow through BH-BH mergers (Dubois et al. 2014). For central cluster galaxies BH-BH mergers, in which one of the BHs does not get ejected from the center, occurs more frequently than in field or satellite galaxies (see Yoo & Miralda-Escudé 2004, and references therein)]. In addition, BCGs undergo many dry mergers. During these gas-poor mergers, the star formation is less likely to be induced, but the central BH will still grow due to the BH-BH merger (Volonteri & Ciotti 2013). These processes together could result in the higher BH masses of BCGs. Therefore it is possible that mergers aid the growth of BHs in BCGs.

Cold gas flows that directly feed the BH could also play a role in aiding the growth of BHs. Cold gas flows may occur within a radius occupied by the BCG (Reisenegger et al. 1996), if the cooling time of the gas is shorter than the Hubble-timescale. While subsonic cold flows may enhance star formation (see O’Dea et al. 2010, and references therein), many BCGs with cooling flows do not show signatures of active star formation. It is possible that the low-angular momentum gas flows do not give rise to significant star-formation, but support the rapid growth of BHs. Three clusters exhibit cooling flows in our sample, A1795, A2597 and Hydra, which cover a broad range of cluster temperatures with $kT = 1.72 - 6.07$ keV (O’Dea et al. 2004; Rafferty et al. 2006). The inferred mass of these BHs exceeds the expected value from the $M_{\text{BH}} - M_{\text{bulge}}$ relation of McConnell & Ma (2013), these particular clusters are $3.5\sigma - 4.0\sigma$ outliers from the local $M_{\text{BH}} - M_{\text{bulge}}$ scaling relation. In addition, Rafferty et al. (2006) examined the star formation rate and BH growth rate of these clusters, and concluded that for Hydra the BH is growing faster than expected from the relation of Magorrian et al. (1998). We also examined the location of these BHs on the $M_{\text{BH}} - kT$ and $M_{\text{BH}} - M_{\text{bulge}}$ relations. We find that all three are within $1\sigma_{\text{intrinsic}}^y$ of the $M_{\text{BH}} - kT$ relation. However, they are $2\sigma_{\text{intrinsic}}^y$ above our best-fit $M_{\text{BH}} - M_{\text{bulge}}$ relation. Overall, these results are consistent with the findings of Rafferty et al. (2006). Therefore, it is feasible that low angular momentum cold flows

play a notable role in fueling the growth of BHs in BCGs. This is in slight contradiction with the results found in Section 4.4, where we observed that CC clusters do not host significantly larger BHs than NCC ones. However, our sample only has three clusters with distinct cooling flows, therefore any dependence of the $M_{\text{BH}} - kT$ relation on CC properties may have been washed out due to the sample splitting process.

6. CONCLUSIONS

In this work, we investigated the relationship between cluster mass, BCG stellar mass, and BH mass. The main results can be summarized as follows:

- We studied a sample of 71 galaxy clusters in the redshift range of $z = 0.006 - 0.29$. The BH mass of the BCGs was inferred from the Fundamental Plane relation and the total mass of the galaxy clusters was traced through the temperature of the ICM.
- We concluded that the BH mass of BCGs significantly exceeds that expected from the local scaling relations, implying that additional processes aid the growth of these BHs. We also derived scaling relations between the BH mass, BCG stellar mass, and galaxy cluster mass.
- We found that the best-fit $M_{\text{BH}} - kT$ relation is steeper than that of Bogdán et al. (2018) and a larger scatter is present. Using Monte Carlo simulations we determined that most of this scatter may originate from the intrinsic scatter of the Fundamental Plane relation.
- We split the galaxy cluster sample using different criteria, and explored whether cool core and non-cool core clusters exhibit a different $M_{\text{BH}} - kT$ relation. However, we did not find a statistically significant difference, suggesting the BHs in BCGs do not undergo different evolution on CC and NCC clusters.
- We discussed the potential causes of the unexpected growth in these BHs, from BH-BH mergers up to cluster-cluster mergers and cooling flows. Some clusters in our sample exhibited these features. Hence we compared their BH masses to the relations we found in section 4.1, which showed that these processes may have some influence over the aided growth of BHs in BCGs. However due to the small number of objects in our sample displaying either a cluster-cluster merger or a cooling flow are small, we cannot definitively say to what

extent the effect is that these processes have. We conclude that in order to test the effects of these processes, we will need to probe galaxy evolution simulations.

We thank Vinay Kashyap and the Statistical Consulting Service of the Harvard Statistics Department for helpful discussion about the fitting procedures. This research has made use of Chandra data provided by the

Chandra X-ray Center (CXC). The publication makes use of software provided by the CXC in the application package CIAO. In this work the NASA/IPAC Extragalactic Database (NED) has been used. Á.B. acknowledges support from the Smithsonian Institute. L.L. acknowledges support from the Chandra X-ray Center through NASA contract NNX17AD83G. M.V. acknowledges funding from the European Research Council under the European Communitys Seventh Framework Programme (FP7/2007-2013 Grant Agreement no. 614199, project BLACK).

REFERENCES

- Akritas, M. G. , Bershad, M. A. 1996, *AJ*, 470, 706
- Anders, E. , Grevesse, N. 1989, *GeoCoA*, 53, 197
- Arnaud, K. A. 1996, *Astronomical Data Analysis Software and Systems V*, A.S.P. Conference Series, 101, 17
- Bassini, L. and Rasia, E. and Borgani, S. and Ragone-Figueroa, C. and Biffi, V. and Dolag, K. and Gaspari, M. and Granato, G. L. and Murante, G. and Taffoni, G. and Tornatore, L. 2019, *A&A*, submitted
- Bell, E. F. and McIntosh, D. H. and Katz, N. and Weinberg, M. D. 2003, *ApJS*, 149, 289
- Bernardi, M. and Hyde, J. B. and Sheth, R. K. and Miller, C. J. and Nichol, R. C. 2007, *AJ*, 133, 1741
- Bogdán, A. and Lovisari, L. and Volonteri, M. and Dubois, Y. 2018, *ApJ*, 852, 131
- Burke, C., Collins, C. A., 2013, *MNRAS*, 434, 2856
- Cattaneo, A. and Faber, S. M. and Binney, J. and Dekel, A. and Kormendy, J. and Mushotzky, R. and Babul, A. and Best, P. N. and Bruggen, M. and Fabian, A. C. and Frenk, C. S. and Khalatyan, A. and Netzer, H. and Mahdavi, A. and Silk, J. and Steinmetz, M. and Wisotzki, L. 2009, *Nature*, 460, 213
- Cheung, E. and Bundy, K. and Cappellari, M. and Pierani, S. and Rujopakarn, W. and Westfall, K. and Yan, R. and Bershad, M. and Greene, J. E. and Heckman, T. M. and Drory, N. and Law, D. R. and Masters, K. L. and Thomas, D. and Wake, D. A. and Weijmans, A. M. and Rubin, K. and Belfiore, F. and Vulcani, B. and Chen, Y. M. and Zhang, K. and Gelfand, J. D. and Bizyaev, D. and Roman-Lopes, A. and Schnieder, D. P. 2016, *Nature*, 533, 504
- Crawford, C. S. and Allen, S. W. and Ebeling, H. and Edge, A. C. and Fabian, A. C. 1999, *MNRAS*, 306, 857
- Croton, D. J. and Springel, V. and White, D. M. S. and De Lucia, G. and Frenk, C. S. and Gao, L. and Jenkins, A. and Kauffmann, G. and Navarro and Yoshida, N. 2006, *MNRAS*, 365, 11
- DeGraf, C. and DiMatteo, T. and Treu, T. and Feng, Y. and Woo, J. H. and Park, D. 2015, *MNRAS*, 454, 913
- Di Matteo, T. and Springel, V. and Hernquist, L. 2005, *Nature*, 433, 604
- Dubois, Y. and Volonteri, M. and Silk, J. 2014, *MNRAS*, 1590, 440
- Ettori, S. and Donnarumma, A. and Pointecouteau, E. and Reiprich, T. H. and Giodini, S. and Lovisari, L. 2013, *SSRv*, 177, 119
- Faber, S. M. and Willmer, C. N. A. and Wolf, C. and Koo, D. C. and Weiner, B. J. and Newman, J. A. and Im, M. and Coll, A. L. and Conroy, C. and Cooper, M. C. and Davis, M. and Finkbeiner, D. P. and Gerke, B. F. and Gebhardt, K. and Groth, E. J. and Guharthakurta, P. and Harker, J. and Kaiser, N. and Kassin, S. and Kleinheinrich, M. and Konidaris, N. P. and Kron, R. G. and Lin, L. and Luppino, G. and Madgwick, D. S. and Meisenheimer, K. and Noeske, K. G. and Phillips, A. C. and Sarajedini, V. L. and Schiavon, R. P. and Simard, L. and Szalay, A. S. and Vogt, N. P. and Yan, R. 2007, *ApJ*, 665, 265
- Fabian, A. C., 1999, *MNRAS*, 308, L39
- Fabian, A. C. and Nulsen, P. E. J. and Canizares, C. R. 1984, *Nature*, 310, 733
- Falcke, H. and Körding, E. and Markoff, S. 2004, *A&A*, 414, 895
- Ferrarese, L. and Merritt, D. 2000, *ApJL*, 539, L9
- Fruscione, A. and McDowell, J. C. and Allen, G. E. and Brickhouse, N. S. and Burke, D. J. and Davis, J. E. and Durham, N. and Elvis, M. and Galle, E. C. and Harris, D. E. and Huenemoerder, D. P. and Houck, J. C. and Ishibashi, B. and Karovska, M. and Nicastro, F. and Noble, M. S. and Nowak, M. A. and Primini, F. A. and Siemiginowska, A. and Smith, R. K. and Wise, M. 2006, *Proc. SPIE*, 6270, 62701V
- Gaspari, M., Sadowski, A. 2017, *ApJ*, 837, 149

- Gebhardt, K. and Bender, R. and Bower, G. and Dressler, A. and Faber, S. M. and Filippenko, A. V. and Green, R. and Grillmair, C. and Ho, L. C. and Kormendy, J. and Lauer, T. R. and Magorrian, J. and Pinkney, J. and Richstone, D. and Tremaine, S. 2000, *ApJL*, 539, L13
- Gültekin, K. and Cackett, E. M. and Miller, J. M. and Di Matteo, T. and Markoff, S. and Richstone, D. O. and Douglas, O. 2009, *A&A*, 456, 404
- Häring, N. and Rix, H. W. 2004, *ApJL*, 604, L89
- Hickox, R. C. and Markevitch, M. 2006, *ApJ*, 645, 95
- Hlavacek-Larrondo, J. and Fabian, A. C. and Edge, A. C. and Hogan, M. T. 2012, *MNRAS*, 424, 224
- Hogan, M. T. and Edge, A. C. and Hlavacek-Lorrondo, J. and Grainge, K. J. B. and Hamer, S. L. and Mahony, E. K. and Russell, H. R. and Fabian, A. C. and McNamara, B. R. and Wilman, R. J. 2015, *MNRAS*, 453, 1201
- Hopkins, P. F. and Hernquist, L. and Cox, T. J. and Di Matteo, T. and Robertson, B. and Springel, V. 2006, *ApJS*, 163, 1
- Horner, D. J. and Mushotzky, R. F. and Scharf, C. A. 1999, *ApJ*, 520, 78
- Hudson, D. S. and Mittal, R. and Reiprich, T. H. and Nulsen, P. E. J. and Andernach, H. and Sarazin, C. L. 2010, *A&A*, 513, A37
- Kalberla, P. M. W. and Burton, W. B. and Hartmann, D. and Arnal, E. M. and Bajaja, E. and Morras, R. and Pöppel, W. G. L. 2005, *A&A*, 440, 775
- Kaviraj, S. 2014, *MNRAS*, 440, 2944
- King, A., 2003, *ApJL*, 596, L27
- Körding, E. and Falcke, H. and Corbel, S. 2006, *A&A*, 456, 439
- Kormendy, J., and Ho, L. C. 2013, *ARA&A*, 51, 511
- Lovisari, L., Reiprich, T. H., & Schellenberger, G. 2015, *A&A*, 573, A118
- Lovisari, L. and Forman, W. R. and Jones, C. and Ettori, S. and Andrade-Santos, F. and Arnaud, M. and Democles, J. and Pratt, G. W. and Randall, S. and Kraft, R. 2017, *ApJ*, 846, 1
- Magorrian, J. and Tremaine, S. and Richstone, D. and Bender, R. and Bower, G. and Dressler, A. and Faber, S. M. and Gebhardt, K. and Green, R. and Grillmair, C. and Kormendy, J. and Lauer, T. 1998 *AJ*, 115, 2285
- McConnell, N. J. and Ma, C. P. and Murphey, J. D. and Gebhardt, K. and Lauer, T. R. and Graham, J. R. and Shelley, A. and Richstone, D. O. 2012, *ApJ*, 756, 179
- McConnell, N. J., Ma, C. P., 2013, *ApJ*, 764, 184
- McConnell, N. J. and Ma, C. P. and Gebhardt, K. and Wright, S. A. and Murphey, J. D. and Lauer, T. R. and Graham, J. R. and Richstone, D. O. 2011, *Nature*, 480, 215
- Merloni, A. and Heinz, S. and di Matteo, T. 2003, *MNRAS*, 345, 1057
- Mezcua, M. and Hlavacek-Lorrondo, J. and Lucey, J. R. and Hogan, M. T. and Edge, A. C. and McNamara, B. R. 2018, *MNRAS*, 474, 1342
- Mittal, R. and Hudson, D. S. and Reiprech, T. H. and Clarke, T. 2009, *Å*, 501, 835
- O'Dea, K. P. and Quillen, A. C. and O'Dea, C. P. and Tremblay, G. R. and Snios, B. T. and Baum, S. A. and Christiansen, K. and Edge, A. C. and Donahue, M. and Voit, G. M. 2010, *ApJ*, 719, 1619
- O'Dea, C. P. and Baum, S. A., and Mack, J. and Koekemoer, A. M. and Laor, A. 2004, *ApJ*, 612, 131
- Plotkin, R. M. and Markoff, S. and Kelly, B. C. and Körding, E. and Anderson, S. F. 2012, *MNRAS*, 419, 267
- Rafferty, D. A. and McNamara, B. R. and Nulsen, P. E. J. and Wise, M. W. 2006, *ApJ*, 652, 216
- Reisenegger, A. and Miralda-Escude, J. and Waxman, E. 1996, *ApJL*, 457, 11
- Richstone, D. and Ajhar, E. A. and Bender, R. and Bower, G. and Dressler, A. and Faber, S. M. and Filippenko, A. V. and Gebhardt, K. and Green, R. and Ho, L. C. and Kormendy, J. and Lauer, T. R. and Magorrian, J. and Tremaine, S. 1998, *Nature*, 385, A14
- Santos, J. S. and Rosati, P. and Tozzi, P. and Böhringer, H. and Ettori, S. and Bignamini, A. 2008, *A&A*, 483, 35
- Schellenberger, G. and Reiprich, T. H. and Lovisari, L. and Nevalainen, J. and David, L. 2015, *Å*, 575, 30
- Sepp, T., Gramann, M. 2013, *arXiv*, 1309, 7786
- Shankar, F. and Lapi, A. and Salucci, P. and De Zotti, G. and Danese, L. 2006, *ApJ*, 643, 14
- Somerville, R. S. and Hopkins, P. F. and Cox, T. J. and Robertson, B. E. and Hernquist, L. 2008, *MNRAS*, 391, 481
- Vikhlinin, A. and Burenin, R. and Forman, W. R. and Jones, C. and Hornstrup, A. and Quintana, H. 2007, *Heating versus Cooling in Galaxies and Clusters of Galaxies*, *Eso Astrophysics Symposia*, 48
- Volonteri, M., Ciotti, L., 2013, *ApJ*, 1, 768
- Yoo, J., Miralda-Escudé, J., 2004, *ApJL*, L25, 614

APPENDIX

A.

Here we display images of each cluster as seen in the X-ray as well as displaying the annulus within which the final spectra were extracted.

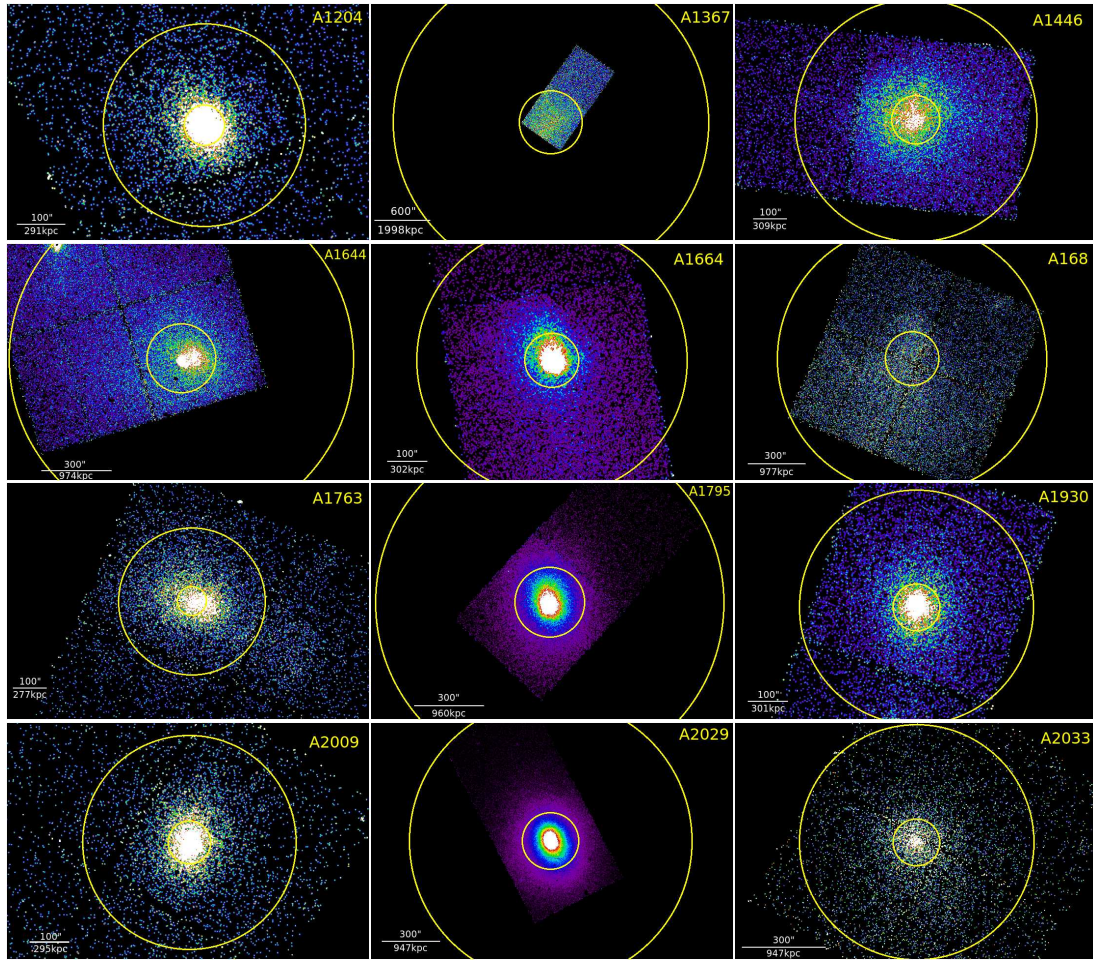


Figure 6.

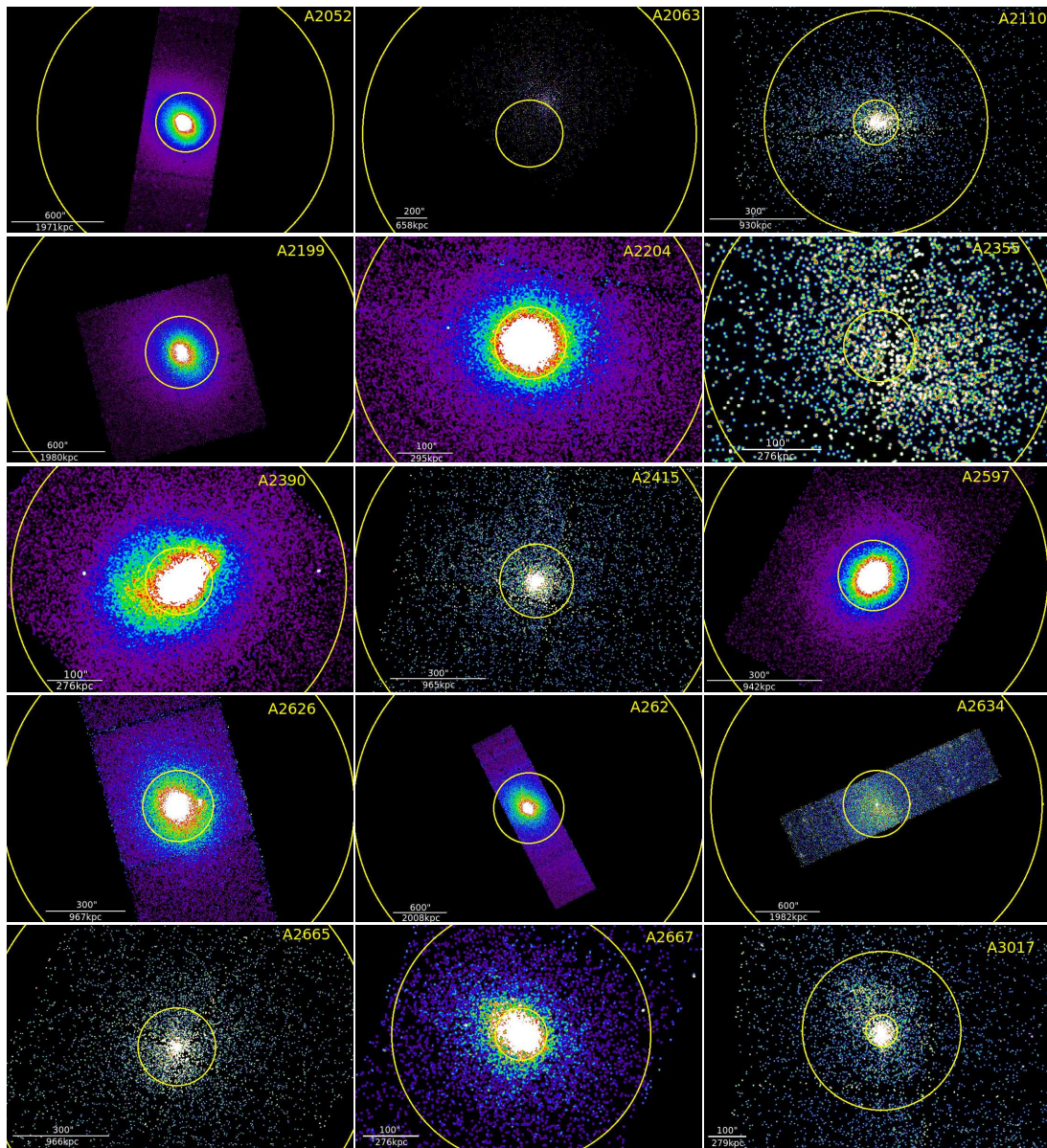


Figure 7.

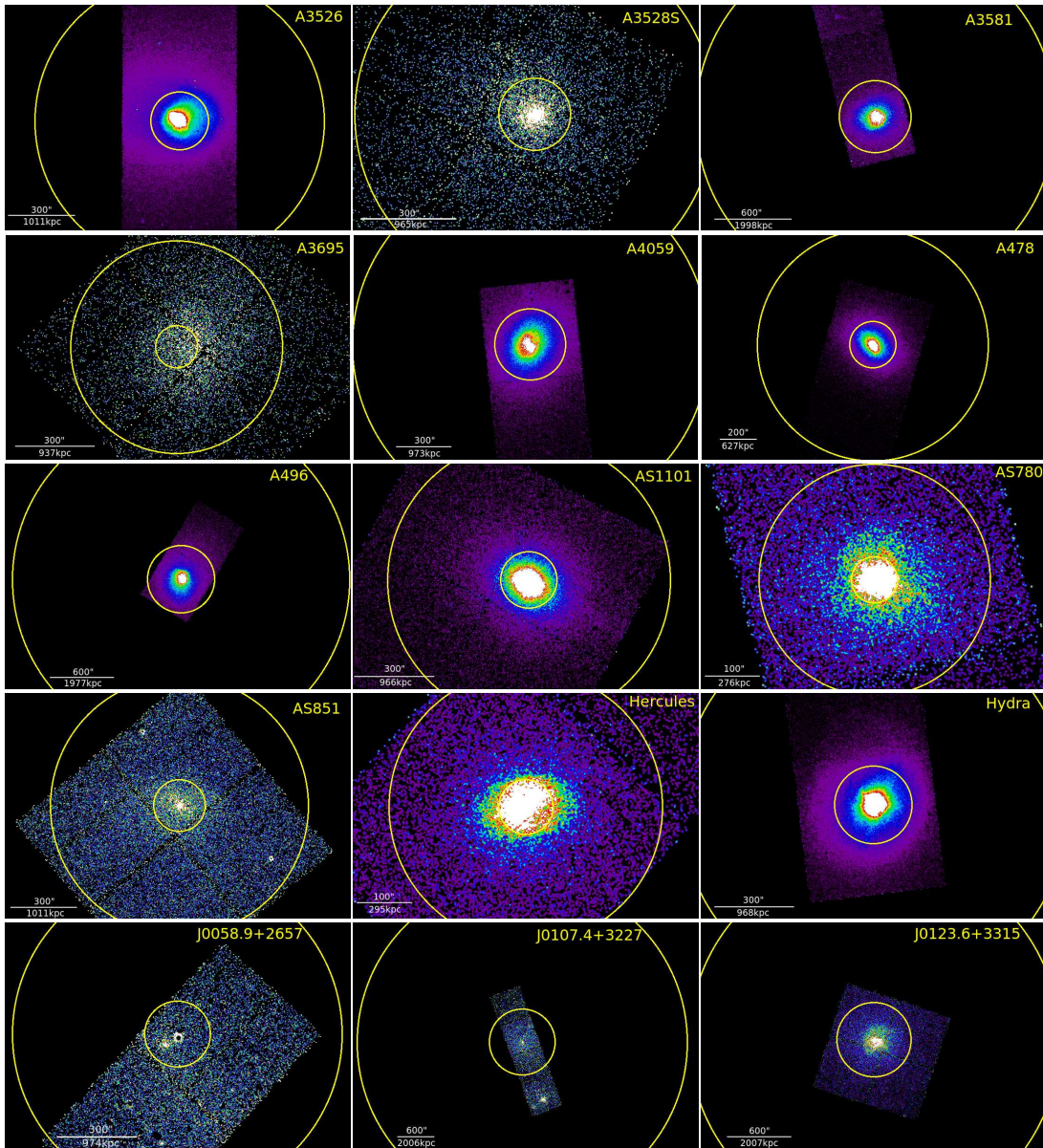


Figure 8.

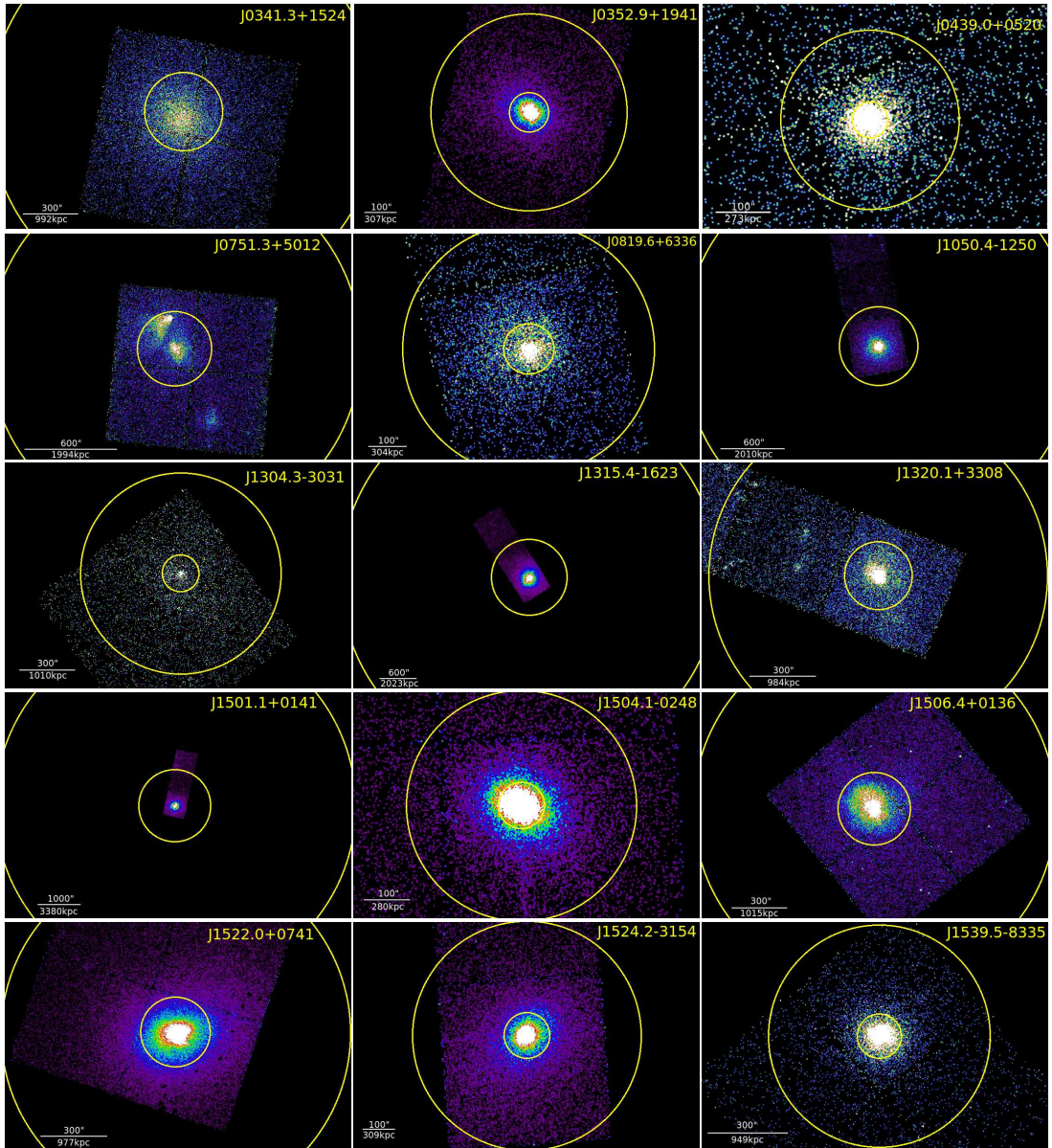


Figure 9.

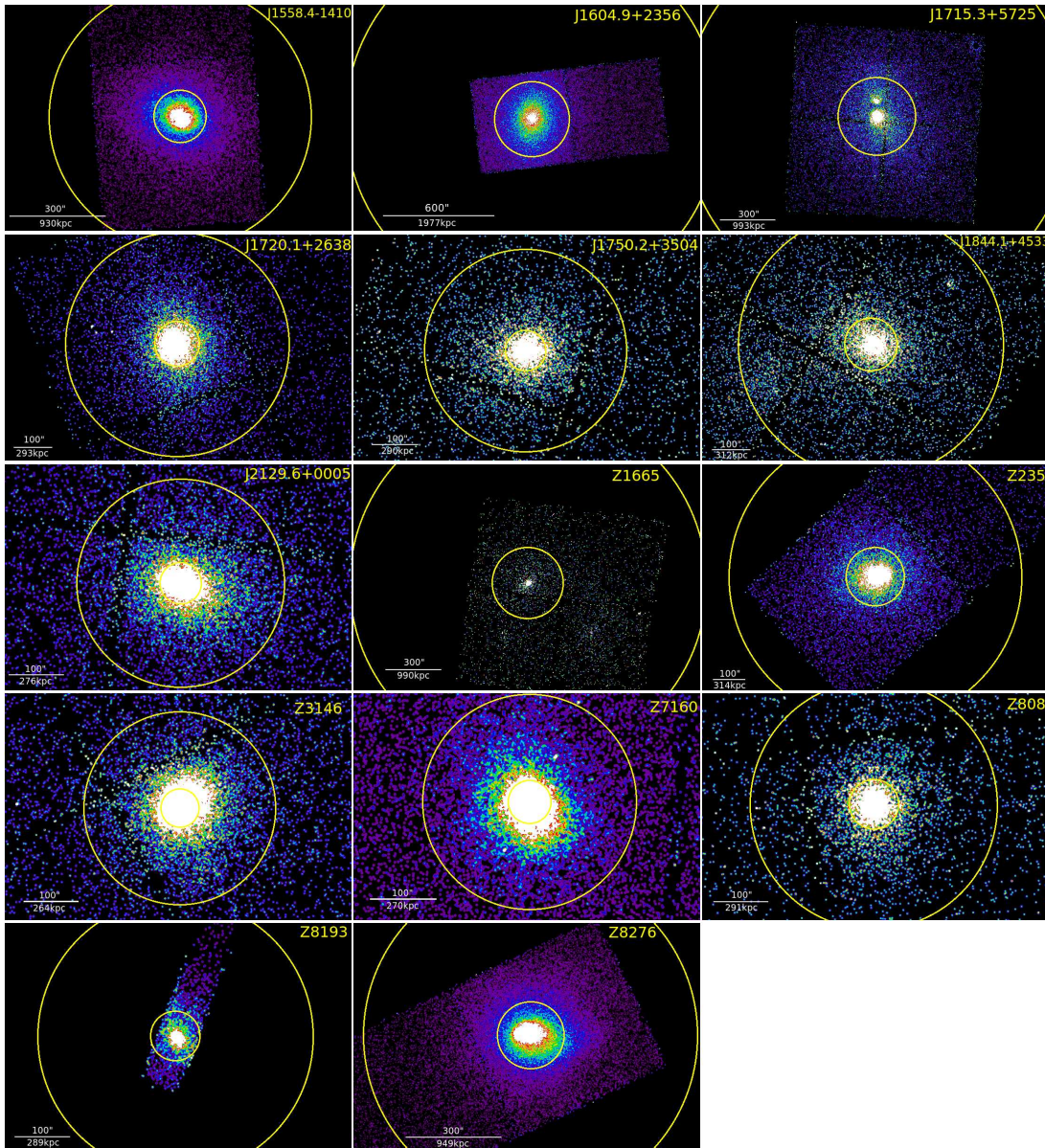


Figure 10.